

Proceedings of the

3rd NIRS-SNU

Workshop on Nuclear Medicine Imaging Science and Technology

March 28, 2014

National Institute of Radiological Sciences, Chiba, Japan



強力ながん診断法などとして注目されるPET(陽電子断層撮影法)。医用放射線イメージング技術に関する、放医研とソウル大学との合同ワークショップを開催します。日本と韓国からの招待講演と、ドイツLMUのParodi氏による特別講演を交え、最先端研究について議論します。みなさまのご参加をお待ちしています。

Venue

Lecture Hall, Research Building for Charged Particle Therapy, National Institute of Radiological Sciences (NIRS), Chiba, Japan
<http://www.nirs.go.jp/ENG/about/map.shtml>
 (放医研 重粒子治療推進棟 2階 大会議室)

Chair organizers

Jae Sung Lee, Ph.D., Associate Professor,
 Seoul National University (SNU) College of Medicine

Taiga Yamaya, Ph.D., Team Leader,
 National Institute of Radiological Sciences (NIRS)

Registration: free (e-mail to jpet@nirs.go.jp)

Language: English

This workshop was supported by JSPS and NRF under the Japan - Korea Basic Scientific Cooperation Program.

3rd NIRS-SNU

Workshop on Nuclear Medicine Imaging Science and Technology

March 28, 2014 (Friday) 13:00-18:30 NIRS

Opening address 13:00 Yoshiharu Yonekura NIRS President

Presentations from NIRS and SNU Moderator: Takayuki Obata (NIRS)

13:10	Updates in PET imaging physics at NIRS	Taiga Yamaya	NIRS
13:35	Progress in PET and PET/MR researches at SNU	Jae Sung Lee	SNU
14:00	Development of a head RF-coil with DOI detectors for PET/MRI measurement	Fumihiko Nishikido	NIRS
14:15	Prototype digital SiPM-based PET detector pair with continuous depth-of-Interaction encoding capability	Min Sun Lee	SNU
14:30	Imaging simulation of a helmet-PET with a jaw detector	Hideaki Tashima	NIRS
14:45	Noninvasive linear methods for human [11C]ABP688 PET	Seongho Seo	SNU

Special lecture Moderator: Taiga Yamaya (NIRS)

15:00	Unconventional imaging in ion beam therapy: status and perspectives	Katia Parodi	LMU
15:30	Break		

Invited talks Moderator: Hiroshi Ito (NIRS)

16:00	Intraoperative molecular imaging probes	Seong Jong Hong	Eulji Univ.
16:30	Development of PET and multi-modality imaging systems based on new concepts	Seiichi Yamamoto	Nagoya Univ.
17:00	Approach of hybrid PET imaging for improved quantification	Kyeong Min Kim	KIRAMS
17:30	Development of flexible experimental and image database system	Hiroshi Watabe	Tohoku Univ.

Discussion 18:00 Chair: Yasuhisa Fujibayashi (NIRS)

Closing remarks 18:20 Makoto Akashi NIRS Executive Director



主催：独立行政法人放射線医学総合研究所

助成：独立行政法人日本学術振興会・韓国研究財団 二国間交流事業

後援：公益社団法人応用物理学会放射線分科会, 独立行政法人科学技術振興機構(JST)研究成果展開事業, 千葉大学
 フロンティア工学センター, 一般社団法人日本医学物理学会, 日本医用画像工学会, 一般社団法人日本核医学会, 独立
 行政法人日本学術振興会放射線科学とその応用第186委員会, 一般社団法人日本磁気共鳴医学会 (50音順)
 千葉県, 千葉市, 公益財団法人ちば国際コンベンションビューロー

参加登録: jpet@nirs.go.jpへお名前とご所属をお知らせください。(参加無料)

千葉県PRマスコットキャラクター チューバくん
 (千葉県許諾 第A836-1号)



Table of Contents

		Page
(1) Updates in PET imaging physics at NIRS	T. Yamaya	2
(2) Progress in PET and PET/MR researches at Seoul National University	J.S. Lee	7
(3) Development of a head RF-coil with DOI detectors for PET/MRI measurement	F. Nishikido, et al.	10
(4) Prototype digital SiPM-based PET detector pair with continuous depth-of-interaction encoding capability	M.S. Lee, et al.	14
(5) Imaging simulation of a helmet-PET with a jaw detector	H. Tashima, et al.	18
(6) Noninvasive linear methods for human [11C]ABP688 PET	S. Seo, et al.	23
(7) Unconventional imaging in ion beam therapy: status and perspectives	K. Parodi	29
(8) Intraoperative molecular imaging probes	S.J. Hong, et al.	33
(9) Development of PET and multi-modality imaging systems based on new concepts	S. Yamamoto	39
(10) Approach of hybrid PET imaging for improved quantification	K.M. Kim, et al.	41
(11) Development of flexible experimental and image database system	H. Watabe	46

(1) Updates in PET imaging physics at NIRS

Taiga Yamaya

Molecular Imaging Center, National Institute of Radiological Sciences, Japan

Abstract

This paper summarizes research updates in 2013 about PET imaging physics at NIRS, such as OpenPET and X'tal cube as well as PET/MRI, brain PET and entire-body PET.

1. Introduction

Positron emission tomography (PET) plays important roles in cancer diagnosis, neuroimaging and molecular imaging research; but potential points remain for which big improvements could be made, including spatial resolution, sensitivity and manufacturing costs. For example, the sensitivity of present PET scanners does not exceed 10%. This means that more than 90% of the gamma-rays emitted from a subject are not utilized for imaging. Therefore, research on next generation PET technologies remains a hot topic worldwide.

The Imaging Physics Team at National Institute of Radiological Sciences (NIRS) has carried out basic studies on radiation detectors, data acquisition systems, image reconstruction algorithms and data correction methods to improve image quality and quantity in nuclear medicine as well as exploring innovative systems.

A depth-of-interaction (DOI) detector, for which various methods have been studied, will be a key device to get any significant improvement in sensitivity while maintaining high spatial resolution. We have developed 4-layered DOI detectors based on a light sharing method^{[1][2]}. One the successful proof-of-concept was the “jPET” project, in which we developed brain prototype PET with our DOI detectors; almost uniform spatial resolution around 2mm for all over the field-of-view was obtained with iterative image reconstruction with geometrically defined system matrix^[3]. We have also succeed to upgrade the DOI detector to have better spatial resolution with cheaper production costs: successful identification of 32 x 32 x 4 array of LYSO crystals sized in 1.45 x 1.45 x 4.5 mm³ with a 64ch PMT (H8500, Hamamatsu Photonics K.K., Japan)^[4], which has enabled Shimadzu’s new products of positron emission mammography (PEM).

DOI measurement also has a potential to expand PET application fields because it allows for more flexible detector arrangement. As an example, we are developing the world’s first, open-type PET geometry “OpenPET”, which is expected to lead to PET imaging during treatment^[5]. The DOI detector itself continues to evolve with the help of recently developed semiconductor photodetectors, often referred to as silicon photomultipliers (SiPMs)^[15]. We are developing a SiPM-based DOI detector “X’tal cube” to achieve sub-mm spatial resolution, which is reaching the theoretical limitation of PET imaging^[6].

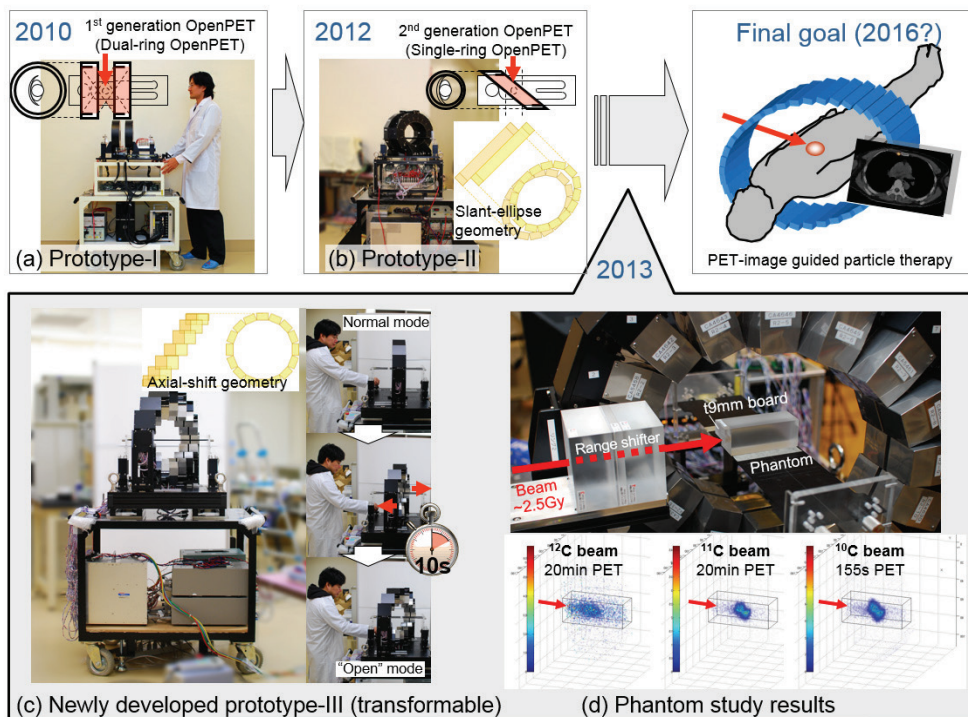


Figure 1 Concepts and small prototypes of the dual-ring OpenPET (a) and the single-ring OpenPET (SROP) (b). As the 3rd prototype, in this year, we developed a transformable SROP prototype (c), and we carried out in-beam imaging test at HIMAC (d).

2. Development of the OpenPET: a future PET for therapy imaging

We are developing the world's first, open-type 3D PET scanner "OpenPET". In addition to the effect to extend axial field-of-view with the limited number of detectors, OpenPET is expected to enable PET-image guided particle therapy such as in situ dose verification and direct tumor tracking^{[32][34]}.

Our initial idea was a dual-ring Open PET (DROP) geometry to visualize a physically opened space between two detector rings^[5]. We developed a small prototype of the DROP^{[7][18]} (Figure 1 (a)). In the last year, we proposed a second-generation geometry, single-ring OpenPET (SROP), which is more efficient than DROP in terms of manufacturing cost and sensitivity^[8]. The detector ring of the SROP geometry is a cylinder shape, both ends of which were cut by parallel slant planes. Arrangement of rectangular block detectors was based on a slanted ellipse (SE) geometry, where oval detector rings are slanted and stacked (Figure 1 (b))^{[14][33]}.

In this year, we developed another SROP prototype based on a new detector arrangement with an axial shift (AS) function (Figure 1 (c))^{[19][23-24][27]}. The major advantage of this geometry over the previous SE geometry is its transformable capability; it can be used as a conventional (i.e., non-open) PET when in-beam PET measurement is not required.

We carried out phantom studies using carbon ion beam (2.5 Gy) (Figure 1 (d)). We also tried direct irradiation of radioisotope beams such as ¹¹C or ¹⁰C as alternatives to measurement of positron emitters produced through fragmentation reaction. The results showed that beam stopping position in the target

could be measured with precision better than 2 mm with the ^{11}C beam irradiation and 20 min PET measurement time. With the ^{10}C beam, PET measurement time could be reduced to 1/10 while maintaining the precision. Following the proof-of-concept obtained by the prototypes, we are now developing a human-size OpenPET, which will be completed by March 2016.

3. The X'tal cube: 1mm isotropic resolution of world records

X'tal (crystal) cube is a future DOI detector we are developing. It consists of multi-pixel photon counters (MPPCs) that are coupled on all sides of a scintillation crystal block, which is segmented into a 3D array of cubes^[9-13]. No reflector is inserted into the crystal block so that scintillation light originating in one of the cubic segment spreads 3-dimensionally and distributes among all MPPCs on the crystal block. In 2012, we achieved 1 mm cubic resolution with $18 \times 18 \times 18$ segments made by 3D laser processing (Figure 2 (a))^[16]. In this year, we investigated stacking scintillator plates with 2D laser segmentation as an alternative and more practical method (Figure 2 (b)). The 2D segmentation of thin scintillators is a method with more tolerance than the 3D segmentation because, for example, we can exchange the scintillator partially in case it causes sudden cracks during processing. In addition, stacks of 2D laser plates is expected to enable analyzing optical condition of laser processing by changing materials between plates in the comparison with the 3D laser block^[26]. We succeeded to achieve 1 mm cubic resolution by stacking 18 plates of 1 mm thickness LYSO plates with 1 mm x 1 mm laser segmentations^[35].

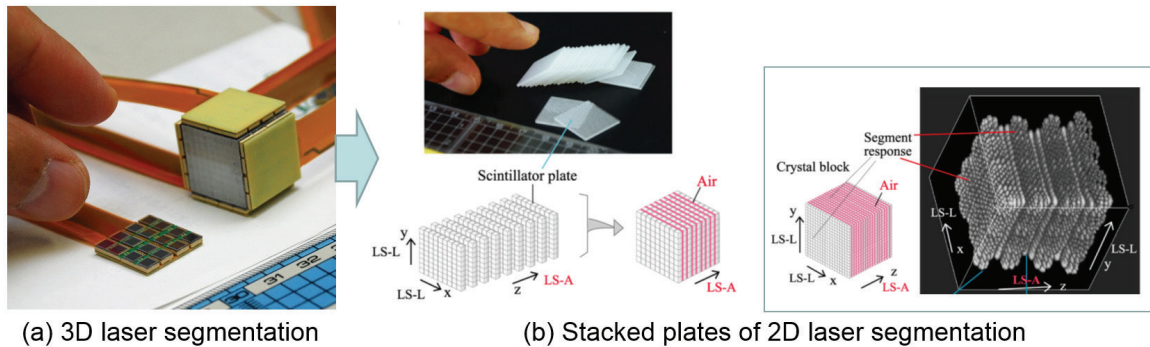


Figure 2 Prototype X'tal cube detectors: a monolithic crystal block with 3D laser segmentation (a) and stacked plates with 2D laser segmentation (b).

4. Other topics

One of recently increasing demands is PET/MRI. We have started a new project to develop a brain PET/MRI by taking advantages of our DOI technologies. Our goal is to develop a RF coil with PET detectors; theoretically it can be applied to any existing MRI systems^{[22][28]}. MRI-based PET attenuation correction is also one of our interests^[29]. For brain imaging, we are designing a helmet-type PET geometry in order to achieve both high imaging performance and reduced costs^[25]. Appropriate geometries for entire-body imaging is also our interest^{[17][30-31]}.

References

- [1] H. Murayama, H. Ishibashi, H. Uchida, T. Omura, T. Yamashita, "Depth encoding multicrystal detectors for PET," *IEEE Trans. Nucl. Sci.*, vol. 45, no. 3, pp. 1152–1157, Jun. 1998.
- [2] N. Inadama, H. Murayama, T. Omura, T. Yamashita, S. Yamamoto, H. Ishibashi et al., "A depth of interaction detector for PET with GSO crystals doped with different amounts of Ce," *IEEE Trans. Nucl. Sci.*, vol. 49, no. 3, pp. 629–633, Jun. 2002.
- [3] Taiga Yamaya, Eiji Yoshida, Takashi Obi, Hiroshi Ito, Kyosan Yoshikawa, Hideo Murayama, "First human brain imaging by the jPET-D4 prototype with a pre-computed system matrix," *IEEE Trans. Nucl. Sci.*, vol. 55, no. 5, pp. 2482-2492, 2008.
- [4] Tomoaki Tsuda, Hideo Murayama, Keishi Kitamura, Taiga Yamaya, Eiji Yoshida, Tomohide Omura, Hideyuki Kawai, Naoko Inadama, and Narimichi Orita, "A Four-Layer Depth of Interaction Detector Block for Small Animal PET," *IEEE Trans. Nucl. Sci.*, vol. 51, no. 5, pp. 2537-2542, 2004.
- [5] Taiga Yamaya, Taku Inaniwa, Shinichi Minohara, Eiji Yoshida, Naoko Inadama, Fumihiko Nishikido, Kengo Shibuya, Chih Fung Lam and Hideo Murayama, "A proposal of an open PET geometry," *Phy. Med. Biol.*, 53, pp. 757-773, 2008.
- [6] Taiga Yamaya, Takayuki Mitsuhashi, Takahiro Matsumoto, Naoko Inadama, Fumihiko Nishikido, Eiji Yoshida, Hideo Murayama, Hideyuki Kawai, Mikio Suga and Mitsuo Watanabe, "A SiPM-based isotropic-3D PET detector X'tal cube with a three-dimensional array of 1 mm³ crystals," *Phys. Med. Biol.*, Vol. 56, pp. 6793-6807, 2011.
- [7] Taiga Yamaya, Eiji Yoshida, Taku Inaniwa, Shinji Sato, Yasunori Nakajima, Hidekatsu Wakizaka, Daisuke Kokuryo, Atsushi Tsuji, Takayuki Mitsuhashi, Hideyuki Kawai, Hideaki Tashima, Fumihiko Nishikido, Naoko Inadama, Hideo Murayama, Hideaki Haneishi, Mikio Suga, Shoko Kinouchi, "Development of a small prototype for a proof-of-concept of OpenPET imaging," *Phys. Med. Biol.*, 56, pp. 1123-1137, 2011.
- [8] Hideaki Tashima, Taiga Yamaya, Eiji Yoshida, Shoko Kinouchi, Mitsuo Watanabe, Eiichi Tanaka, "A single-ring OpenPET enabling PET imaging during radiotherapy," *Phys. Med. Biol.*, 57, pp. 4705-4718, 2012.

Achievements in 2013

(Peer-reviewed full papers)

- [9] Eiji Yoshida, Hideaki Tashima, Naoko Inadama, Fumihiko Nishikido, Takahiro Moriya, Tomohide Omura, Mitsuo Watanabe, Hideo Murayama, Taiga Yamaya, "Intrinsic spatial resolution evaluation of the X'tal cube PET detector based on a 3D crystal block segmented by laser processing," *Radiological Physics and Technology*, vol. 6, no. 1, pp. 21-27, 2013.
- [10] Yoshiyuki Hirano, Naoko Inadama, Eiji Yoshida, Fumihiko Nishikido, Hideo Murayama, Mitsuo Watanabe, Taiga Yamaya, "Potential for reducing the numbers of SiPM readout surfaces of laser-processed X'tal cube PET detectors," *Phys. Med. Biol.*, 58, pp. 1361-1374, 2013.
- [11] Eiji Yoshida, Hiroki Yamashita, Hideaki Tashima, Shoko Kinouchi, Hideo Murayama, Mikio Suga, Taiga Yamaya, "Design study of the DOI-PET scanners with the X'tal cubes toward sub-millimeter spatial resolution," *Journal of Medical Imaging and Health Informatics*, Vol. 3, pp. 131–134, 2013
- [12] Eiji Yoshida, Yoshiyuki Hirano, Hideaki Tashima, Naoko Inadama, Fumihiko Nishikido, Takahiro Moriya, Tomohide Omura, Mitsuo Watanabe, Hideo Murayama, Taiga Yamaya, "The X'tal cube PET detector with a monolithic crystal processed by the 3D sub-surface laser engraving technique: Performance comparison with glued crystal elements," *Nuclear Instruments and Methods in Physics Research A* 723, pp. 83–88, 2013.
- [13] Eiji Yoshida, Hideaki Tashima, Yoshiyuki Hirano, Naoko Inadama, Fumihiko Nishikido, Hideo Murayama, Taiga Yamaya, "Spatial resolution limits for the isotropic-3D PET detector X'tal cube," *Nuclear Instruments and Methods in Physics Research A* 728, pp. 107-111, 2013.
- [14] Eiji Yoshida, Hideaki Tashima, Hidekatsu Wakizaka, Fumihiko Nishikido, Yoshiyuki Hirano, Naoko Inadama, Hideo Murayama, Hiroshi Ito, Taiga Yamaya, "Development of a single-ring OpenPET prototype," *Nuclear Instruments and Methods in Physics Research A*, 729, pp. 800–808, 2013.
- [15] Fumihiko Nishikido, Naoko Inadama, Eiji Yoshida, Hideo Murayama, Taiga Yamaya, "Four-layer DOI PET detectors using a multi-pixel photon counter array and the light sharing method," *Nuclear Instruments and Methods in Physics Research A*, 729, pp. 755–761, 2013.
- [16] Eiji Yoshida, Yoshiyuki Hirano, Hideaki Tashima, Naoko Inadama, Fumihiko Nishikido, Takahiro Moriya, Tomohide Omura, Mitsuo Watanabe, Hideo Murayama, Taiga Yamaya, "Impact of laser-processed X'tal cube detectors on PET imaging in a one-pair prototype system," *IEEE Transactions on Nuclear Science*, Vol. 60, No. 5, 3172-3180, October 2013.
- [17] Eiji Yoshida, Yoshiyuki Hirano, Hideaki Tashima, Naoko Inadama, Fumihiko Nishikido, Hideo Murayama, Hiroshi Ito, Taiga Yamaya, "Feasibility study of an axially extendable multiplex cylinder PET," *IEEE Transactions on Nuclear*

Science, Vol. 60, No. 5, 3227-3234, October 2013.

- [18] Yoshiyuki Hirano, Shoko Kinouchi, Yoko Ikoma, Eiji Yoshida, Hidekazu Wakizaka, Hiroshi Ito, Taiga Yamaya, "Compartmental analysis of washout effect in rat brain: in-beam OpenPET measurement using a ^{11}C beam," Phys. Med. Biol., 58, pp. 8281-8294, 2013.

(Presentation in IEEE NSS-MIC2013)

- [19] T. Yamaya, E. Yoshida, H. Tashima, Y. Nakajima, F. Nishikido, Y. Hirano, N. Inadama, T. Shinaji, H. Haneishi, M. Suga, S. Sato, T. Inaniwa, "Development of an Open-Type PET for 3D Dose Verification in Carbon Ion Therapy," HT3-2 (ORAL).
- [20] N. Inadama, Y. Hirano, F. Nishikido, H. Murayama, M. Nitta, T. Yamaya, "A Convenient Light Guide for Trial Production in Its Optimization Process," J1-3 (ORAL).
- [21] E. Yoshida, H. Tashima, T. Yamaya, "Sensitivity Booster for DOI-PET by Utilizing Compton Scattering Events Between Detector Blocks," M16-14.
- [22] K. Shimizu, M. Suga, A. Tachibana, F. Nishikido, H. Kuribayashi, I. Nakajima, Y. Kawabata, T. Yamaya, T. Obata, "Development of a Novel MR Head Coil Integrated with PET Detectors: Design and Optimization of Shield Boxes," M05-5 (ORAL).
- [23] T. Yamaya, E. Yoshida, H. Tashima, Y. Nakajima, F. Nishikido, Y. Hirano, N. Inadama, H. Ito, T. Shinaji, H. Haneishi, M. Suga, T. Inaniwa, "A Prototype of a Novel Transformable Single-Ring OpenPET," M07-1 (ORAL).
- [24] Y. Nakajima, Y. Hirano, T. Yamaya, E. Yoshida, H. Tashima, S. Sato, T. Inaniwa, T. Kohno, L. Sihver, "Dosimetry by Means of in-Beam PET with RI Beam Irradiation," M07-2 (ORAL).
- [25] H. Tashima, H. Ito, T. Yamaya, "A Proposed Helmet-PET with a Jaw Detector Enabling High-Sensitivity Brain Imaging," M11-11.
- [26] A. Gondo, T. Shinaji, Y. Hirano, E. Yoshida, F. Nishikido, N. Inadama, H. Tashima, T. Yamaya, H. Haneishi, "Optical Simulation of a DOI Detector with a Stack of Planer Scintillators," M11-17.
- [27] E. Yoshida, T. Shinaji, H. Tashima, H. Haneishi, T. Yamaya, "Performance Evaluation of a Transformable Axial-Shift Type Single-Ring OpenPET," M11-7.
- [28] F. Nishikido, T. Obata, N. Inadama, E. Yoshida, M. Suga, K. Shimizu, A. Tachibana, H. Ito, T. Yamaya, "One-Pair Prototype Integrated System of DOI- PET and the RF-Coil Specialized for Simultaneous PET-MRI Measurements," M12-45.
- [29] H. Kawaguchi, Y. Hirano, E. Yoshida, M. Suga, T. Shiraishi, K. Tanimoto, Y. Kimura, T. Obata, H. Ito, T. Yamaya, "A MRI-Based PET Attenuation Correction with μ -Values Measured by a Fixed-Position Radiation Source," M12-52.
- [30] Y. Yin, H. Tashima, E. Yoshida, T. Kon, T. Obi, T. Yamaya, "Proposal of a New OpenPET Based Simultaneous Whole-Body PET/CT Geometry," M12-53.
- [31] I. Isnaini, T. Obi, E. Yoshida, T. Yamaya, "Simulation of Sensitivity and NECR of Entire-Body PET Scanners for Different FOV Diameters," M16-15.
- [32] T. Shinaji, H. Tashima, E. Yoshida, T. Yamaya, H. Haneishi, "Accuracy Improvement of Time Delay Correction Method for PET-Based Tumor Tracking," M21-13.
- [33] Y. Hirano, E. Yoshida, H. Wakisaka, Y. Nakajima, F. Nishikido, H. Ito, T. Yamaya, "Washout Studies of in-Beam Rat Imaging by the 2nd Generation OpenPET Prototype," M21-16.
- [34] H. Tashima, E. Yoshida, T. Shinaji, H. Haneishi, H. Ito, T. Yamaya, "Monte Carlo Simulation of Region-of-Interest Reconstruction for Real-Time Tumor Tracking by OpenPET," M21-25.
- [35] N. Inadama, Y. Hirano, F. Nishikido, H. Murayama, M. Nitta, H. Ito, T. Yamaya, "The X'tal Cube with 1 mm³ Isotropic Resolution Based on a Stack of Laser-Segmented Scintillator Plates," M21-47.
- [36] H. Tashima, T. Yamaya, "Impact of TOF Information in OpenPET Imaging," M22-13.
- [37] F. Nishikido, T. Moritake, H. Ito, T. Yamaya, "A Prototype Real-Time Dose Distribution Monitoring System Using Plastic Scintillators Connected to Optical Fiber for Interventional Radiology," NPO1-29.
- [38] M. Nitta, Y. Hirano, F. Nishikido, N. Inadama, E. Yoshida, H. Tashima, Y. Nakajima, H. Kawai, T. Yamaya, "Activation Measurement for Material Selection of OpenPET Components in Particle Therapy," NPO2-58.

Lab. Members in FY2013

Taiga Yamaya (Team Leader), Naoko Inadama, Eiji Yoshida (Senior Researchers),

Fumihiko Nishikido, Yasunori Nakajima (Researchers), Hidekatsu Wakizaka (Technical Assistant),

Hideaki Tashima (JSPS Research Fellow), Yoshiyuki Hirano (Postdoctoral Fellow),

Tetsuya Shinaji, Munetaka Nitta (Junior Research Associate), Fujino Obata (Assistant), Madoka Ohno (Secretary)

(2) Progress in PET and PET/MR researches at Seoul National University

Jae Sung Lee

Departments of Nuclear Medicine and Biomedical Sciences,
Seoul National University, Korea

Abstract

In this talk, I will introduce the Department of Nuclear Medicine at Seoul National University (SNU) and briefly summarize the research topics performed in Functional and Molecular Imaging System Lab (physics and engineering group).

1. SNU Functional and Molecular Imaging System Lab (FMISL)

In Seoul National University (SNU) Department of Nuclear Medicine, the FMISL is the physics and engineering group led by Prof. Jae Sung Lee, PhD. The research goal that FMISL pursue is to develop the technologies with which we can acquire the biologically relevant and clinically useful information from human body and living animals. Our current research interests included, but are not limited to, novel medical imaging systems, i.e. hybrid PET-MRI scanner, and advanced biomedical image analysis technologies. We are especially focusing on the radiotracer imaging modalities, such as positron emission tomography (PET) and single photon emission computed tomography (SPECT).

Major research projects performed at FMISL through the research grants funded by Korean government includes:

- Image processing techniques for Compton camera and application to molecular imaging (Atomic Energy R&D Program of the Korean Science and Engineering Foundation, 6/1/2005~3/31/2011)
- High resolution small animal PET systems with three-layer scintillation crystals (Basic Research Program of Korean Science and Engineering Foundation, 3/1/2006~2/28/2009)
- Basic GMPD PET detector technology for PET/MRI (Atomic Energy R&D Program of the Korean Science and Engineering Foundation, 3/1/2007~2/28/2010)
- Digital positron emission mammography system (Atomic Energy R&D Program of the Korean Science and Engineering Foundation, 7/1/2008~6/30/2013)
- Core technologies for time-of-flight PET (Atomic Energy R&D Program of the Korean Science and Engineering Foundation, 7/1/2010~6/30/2013)
- Image processing algorithms and software for integrated PET/MRI system (Ministry of Knowledge Economy, 10/1/2007~6/30/2014)

2. Recent progress in PET and PET/MR development

High QE flat-panel PMT-based TOF PET

TOF measurements in PET allow us to restrict the annihilation position probability to a small segment of interest during the back-projection procedure in image reconstruction. Therefore, we can use this TOF information to reduce the noise generated during image reconstruction. The benefit of the TOF information is even more remarkable in low-statistics images, indicating that this technique is useful for reducing the PET scan time or even the radiopharmaceutical injection dose. Further improvements in image quality can be achieved because of the better timing resolution of the PET scanners. Thus, we are developing new TOF PET system with better timing and spatial resolutions than current state-of-art clinical PET scanners. To achieve the goal of this development, we have devised PET detector module that consists of multi-anode flat panel PMTs with high quantum efficiency (~35%) and short transit time spread and $3 \times 3 \times 20$ mm LGSO crystal block. The initial results of PET imaging with a prototype PET ring with 40 detector blocks will be presented.

SiPM-based MR-compatible PET

We have been developing a compact SiPM-based PET insert that is combined with ultra-high field (UHF: 7-T or 9.4-T) small animal dedicated MR scanners to achieve high sensitivity and spatial resolution both in PET and MRI studies. The PET insert consists of 64 LYSO-SiPM detectors arranged in 4 rings of 16 detectors to yield the ring diameter of 62 mm and axial fields-of-view of 55 mm. Each PET detector consists of single 4×4 channel MPPC which is connected to position encoding circuit and temperature sensor, and coupled with 9×9 LYSO crystal array ($1.2 \times 1.2 \times 10$ mm). The insert was shielded to minimize the interference between PET and MRI systems. Initial physical performance tests yielded maximum sensitivity of 4% with 250-750 keV energy window, and intrinsic spatial resolution of less than 1.0 mm. There was almost no change in the homogeneity of MR images of uniform corn-oil phantom by inserting power-on PET scanner into Bruker 7T MR scanner. No change in PET count rate was observed while applying various RF pulse sequences. We have also acquired several sets of simultaneous PET/MR images using them.

Selected Recent Publications

- [1] J. S. Lee, K. W. Kang, PET/MRI. In: E. E. Kim, M. C. Lee, T. Inoue, W-H. Wong, eds. Clinical PET and PET/CT: Principles and Applications. Springer; 2012.
- [2] J. S. Lee, S. J. Hong, Geiger-mode avalanche photodiodes for PET/MRI. In: K. Iniewski, eds. Electronic Circuits for Radiation Detection. CRC Press LLC; 2010:179-200
- [3] S. M. Kim, H. Seo, J. H. Park, C. H. Kim, C. S. Lee, S-J. Lee, D. S. Lee, J. S. Lee, Resolution recovery reconstruction for a Compton camera. Phys. Med. Biol., vol. 58, pp. 2823-2840, 2013
- [4] M. Ito, M. S. Lee, J. S. Lee, Continuous depth-of-interaction measurement in a single-layer pixelated crystal array using a single-ended readout. Phys. Med. Biol., vol. 58, pp. 1269-1282, 2013

- [5] J. H. Kim, J. S. Lee, I. C. Song, D. S. Lee, Comparison of segmentation-based attenuation correction methods for PET/MRI: evaluation of bone and liver standardized uptake value with oncologic PET/CT data. *J. Nucl. Med.*, vol. 53, pp. 1978-1882, 2012
- [6] S. J. Hong, H. G. Kang, G. B. Ko, I. C. Song, J-T. Rhee, J. S. Lee, SiPM-PET with a short optical fiber bundle for simultaneous PET-MR imaging. *Phys. Med. Biol.*, vol. 57, pp. 3869-3883, 2012
- [7] S. Ahn, S. M. Kim, J. Son, D. S. Lee, and J. S. Lee. "Gap compensation during PET image reconstruction by constrained, total variation minimization," *Med. Phys.*, vol. 39, pp. 589-602, 2012
- [8] H. S. Yoon, G. B. Ko, S. I. Kwon, C. M. Lee, M. Ito, I. C. Song, D. S. Lee, S. J. Hong, and J. S. Lee. "Initial results of simultaneous PET/MRI experiments with an MR-compatible silicon photomultiplier PET scanner," *J. Nucl. Med.*, vol. 53, pp. 608-614, 2012
- [9] C. M. Lee, S. I. Kwon, G. B. Ko, M. Ito, H. S. Yoon, D. S. Lee, S. J. Hong, and J. S. Lee, "A novel compensation method for the anode gain non-uniformity of multi-anode photomultiplier tubes," *Phys. Med. Biol.*, vol. 57, pp. 191-207, 2011.
- [10] S. I. Kwon, J. S. Lee, H. S. Yoon, M. Ito, G. B. Ko, J. Y. Choi, S. H. Lee, I. Chan Song, J. M. Jeong, D. S. Lee, and S. J. Hong, "Development of small-animal PET prototype using silicon photomultiplier (SiPM): initial results of phantom and animal imaging studies," *J. Nucl. Med.*, vol. 52, pp. 572-9, 2011.

(3) Development of a head RF-coil with DOI detectors for PET/MRI measurement

F. Nishikido¹, T. Obata¹, K. Shimizu², M. Suga², N. Inadama¹,
A. Tachibana¹, E. Yoshida¹, H. Ito¹, T. Yamaya¹

¹ National Institute of Radiological Sciences, Japan

² Chiba University, Japan

Abstract

We are developing a brain-dedicated PET-MRI system in which four-layer DOI-PET detectors we previously proposed are integrated with the head coil of the MRI. As a first step, we investigated the influences of the four-layer DOI-PET detector and the MRI system on the other modality using a prototype system consisted of a four-layer DOI-PET detector and a prototype RF head coil. As a result, there is no influence by the MRI measurements on the PET imaging in the simultaneous measurement. However, the SNR of the MRI image was degraded in the simultaneous measurement.

1. Introduction

We are developing a brain-dedicated PET-MRI system in which four-layer DOI-PET detectors are integrated with the head coil of the MRI [1]. The DOI-PET detector we previously proposed [2] can be positioned close to an object thanks to the four-layer DOI encoding capability and realize a novel PET-MRI configuration which can achieve high sensitivity with high spatial resolution as shown in fig. 1. In the proposed system, the four-layer DOI detectors are mounted on the birdcage type head coil which consists of a number of rod-shaped coil elements. The scintillation crystals which are permeable to the RF-pulse from the MRI can be positioned closer to the measured object than the coil elements as shown in fig.1. The photo-detectors and front-end circuits inside the shielding boxes to minimize electric noises from the PET detectors and MRI system are positioned outside the coil elements not to block RF-pulses from the head coil elements. As a first step, we investigated the influences of the four-layer DOI-PET detector and the MRI system on the other modality using a prototype system consisted of a four-layer DOI-PET detector and a prototype RF head coil.

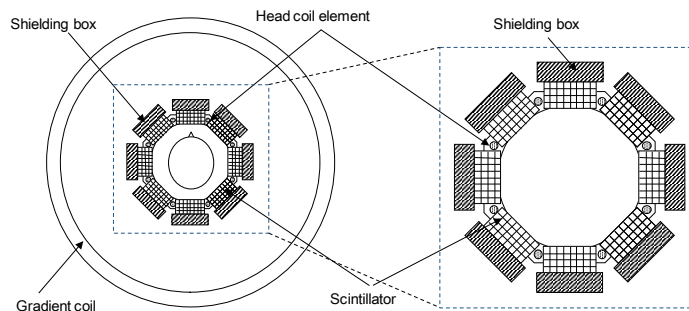
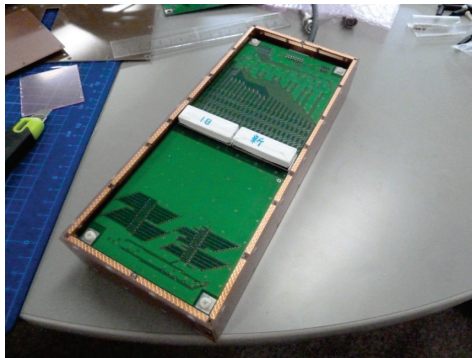


Figure 1. Schematic drawings for the proposed PET-MRI system.

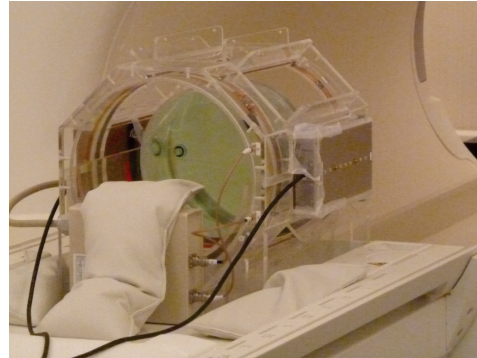
2. Materials and methods

2.1 Prototype system

The prototype system for evaluation of the proposed integrated PET-MRI consisted of the four-layer DOI-PET detector and the prototype head coil. A photograph of the prototype system is shown in fig.2. The prototype DOI-PET detector consisted of six multi-pixel photon counter (MPPC) arrays (S11064-050P, Hamamatsu Photonics K. K.), two scintillator crystal blocks, a readout circuit board and a copper shielding box (fig. 2(a)). Each MPPC array had 4×4 readout pixels. The six MPPC arrays were arranged on a line and soldered onto the readout circuit board. The scintillator blocks consisted of $\text{Lu}_{1.8}\text{Gd}_{0.2}\text{SiO}_5:\text{Ce}$ (LGSO, Hitachi Chemical Co., Ltd., Japan) scintillators arranged in a $12 \times 4 \times 4$ layers and reflectors inserted between them. The size of each crystal element was $2.9 \text{ mm} \times 2.9 \text{ mm} \times 5.0 \text{ mm}$. The reflector was the multilayer polymer mirror (Sumitomo 3M, Ltd.) of 0.065 mm thickness and 98 % reflectivity. A half of each crystal block was positioned outside the shielding box where it projected from a hole ($83 \text{ mm} \times 15 \text{ mm}$) on the top of the box as shown. The 96ch readout signals from all MPPC pixels were reduced to 4 ch signals with a weighted sum circuit and amplified with amplifiers on the readout circuit board. The amplified signals were fed to a data acquisition system to be digitalized and recorded using a Windows PC. The prototype RF head coil was dedicated to a 3.0 T MRI (MAGNETOM Verio, Siemens). The diameter of the coil elements was 27.5 cm. There were eight coil elements and the PET detectors could be mounted on gaps between the coil elements. The four-layer DOI detector was mounted on left side of the prototype head coil.



(a) DOI detector and readout circuit



(b) prototype RF head coil

Figure 2. Photograph of the prototype PET-MRI system.

2.2 Experiments

We evaluated performance of the prototype four-layer DOI detector and influence of PET measurements on MRI images. The PET detectors, the head coil and cables were in the MRI room and the data acquisition system and power supplies for the MPPC and the preamplifiers were outside it. The length of the cables for signal readout and power supply were 10 m. No temperature control was applied to the PET detectors during the experiment. Energy resolution and 2D position histograms were measured for 511keV annihilation radiations from a ^{22}Na point-like source with and without MRI measurements. Gradient echo ($\text{TR}=7300\text{ms}$, $\text{TE}_1=2.46\text{ms}$, $\text{TE}_2=7.38\text{ms}$) and spin echo ($\text{TR}=5000\text{ms}$, $\text{TE}=94\text{ms}$) methods were used in

simultaneous measurements. We also evaluated influence of the PET measurements on the MRI images. A cylindrical phantom (nickel chloride solution, $\Phi 220\text{mm} \times 120\text{mm}$ length) was positioned at the center of the field of view. Magnitude images of the cylindrical phantom were measured by the spin echo method (TR=5000ms, TE= 156ms) to evaluate the SNR of the MRI images for the simultaneous measurements.

3. Results and Discussion

Figure 3 shows 2D position histograms for uniform irradiation of the ^{22}Na point source with and without MRI measurements by the gradient echo (GRE) and spin echo (SE) methods. The spot corresponding with two $12 \times 4 \times 4$ crystal blocks are clearly represented shown in one flood histogram in three position histograms. Comparison of the three position histograms shows no degradation of crystal identification performance for all MRI sequences. The energy resolutions of single crystal elements obtained by applying ROIs to the position histograms are shown in table 1. Difference between the average energy resolutions for the crystal elements in each layer with and without PET measurement is lower than 0.3 percentage point. These results show the influence of the MRI on the energy information of the PET detector is negligible in the simultaneous measurements.

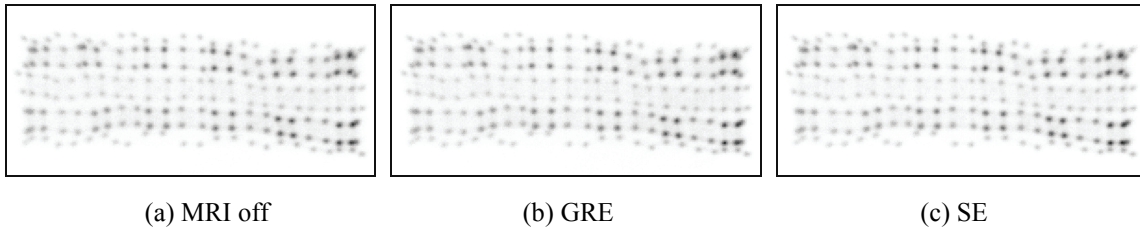


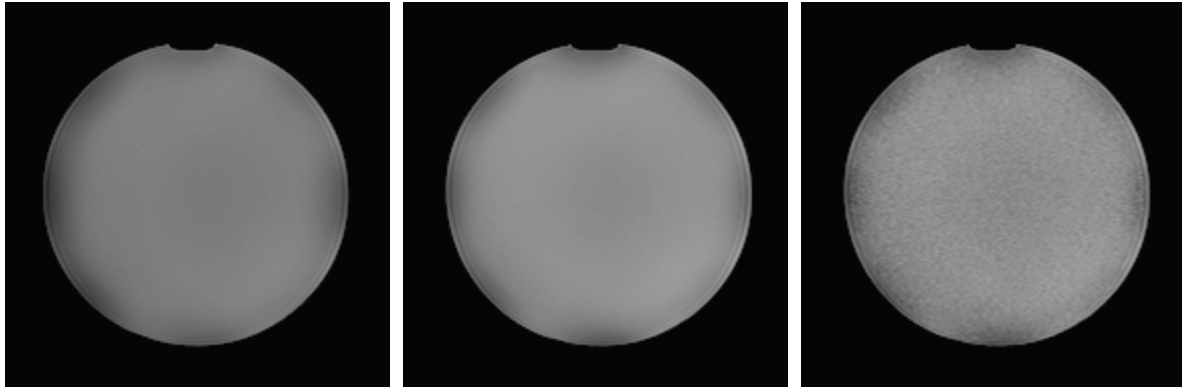
Figure 3. 2D position histograms for uniform irradiation of 511 keV annihilation radiations (a) without MRI measurement, (b) with MRI measurement (gradient echo) and (c) with MRI measurement (spin echo). The two crystal arrays are represented in the flood histograms.

Table 1. Energy resolutions of the single crystal elements (% FWHM)

	out of MRI	MRI off	MRI off
1st layer	14.4 ± 0.9	14.6 ± 0.9	14.7 ± 1.0
2nd layer	15.1 ± 1.3	15.2 ± 1.2	15.3 ± 1.3
3rd layer	15.8 ± 1.7	16.0 ± 1.7	16.1 ± 1.7
4th layer	18.0 ± 4.0	18.0 ± 4.0	18.1 ± 3.9

Figure 4 shows magnitude images measured for the cylindrical phantom by the spin echo method. The left, center and right figures are obtained in the experiments without the PET detectors, with the PET detectors turned off and with the PET detectors in the simultaneous measurements, respectively. The SNRs of the phantom images by the difference method in the three magnitude images are (a) 247.77, (b) 242.80 and (c) 44.948. The result shows that the electronic circuits in the acquisition system of the PET degrade the SNR

of the MRI images. The noise from the acquisition system enters the MRI room through the signal cables. In addition, even when the PET detectors were turned off, the SNR is slightly degraded since external noises contaminate the MRI signal, passing through the cables from outside the MRI room.



(a) Without PET detectors (b) With PET detectors turned off (c) Simultaneous measurements

Fig 4. Magnitude images measured for the cylindrical phantom by the spin echo method. The left, center and right figures were obtained in the experiments (a) without the PET detectors, (b) with the PET detectors turned off and (c) with simultaneous measurements.

4. Conclusions

We evaluated reciprocal influence between the PET detectors and MRI images using the prototype system. As a result, although there is no influence by the MRI measurements on the PET imaging in the simultaneous measurement, the SNR of the MRI image was degraded in the simultaneous measurement. We are investigating effective shielding method [3] and planning a one-ring prototype which consists of eight PET detectors for evaluation of PET imaging performance in the proposed configuration.

Acknowledgments

The part of this work was supported by JSPS KAKENHI Grant Number 24390295 and funds from the Japan Science and Technology Agency (JST) for the project “Development of Systems and Technology for Advanced Measurement and Analysis.”

References

- [1] F. Nishikido, A. Tachibana, T. Obata, et al., " Feasibility study for a PET detector integrated with an RF coil for PET-MRI", 2011 IEEE Nucl. Sci. Symp. Conf. Rec., M13-7, 2011.
- [2] T. Tomoaki, H. Murayama, K. Kitamura, et al. "A Four-Layer Depth of Interaction Detector Block for Small Animal PET", IEEE Trans. Nucl. Sci. 51, pp.2537-42, 2004.
- [3] K. Shimizu, M. Suga, A. Tachibana, et al., "Development of a Novel MR Head Coil Integrated with PET Detectors: Design and Optimization of Shield Boxes", 2013 IEEE Nucl. Sci. Symp. Conf. Rec., M05-5, 2013.

(4) Prototype digital SiPM-based PET detector pair with continuous depth-of-interaction encoding capability

Min Sun Lee^{1,2}, Jae Sung Lee^{1,2}

¹ Interdisciplinary Program in Radiation Applied Life Science, Seoul National University, Korea

² Department of Nuclear Medicine, Seoul National University, Korea

Abstract

We have previously proposed depth-of-interaction (DOI) encoding method to extract continuous DOI information with a single-layer pixelated crystal and a single-ended readout using triangular shape reflector (PMB 2010; 2013). Moreover, experimental evaluation of our DOI PET detector composed with $2 \times 2 \times 20$ mm³ pixelated LGSO crystal array and digital silicon photomultipliers (dSiPM, DPC-3200-22-44) of Philips was successfully presented (IEEE 2013). And it showed promising results as a high resolution PET detector.

Here, we present experimental demonstration of a prototype DOI PET ring system by rotating the dSiPM-based PET detector pair. Each DOI PET detector was consisted of 18×18 unpolished LYSO crystal ($1.47 \times 1.47 \times 15$ mm³) and dSiPM. This two prototype DOI PET detectors and positron-emitting sources were placed on 2-AXIS motorized rotation system, to mimic a virtual PET ring system. Diameter of a PET ring system was set to 12.4 cm for the 12-block ring geometry. List mode data was acquired at all detector configurations to obtain sinograms for the reconstruction. Furthermore, simulation studies with full ring geometry were performed to make comparison with our prototype PET system. To evaluate the performance of our prototype DOI PET system, transaxial resolution is planned to be obtained by moving Na-22 point source in radial direction with 1 cm interval. Data will be analyzed with and without DOI correction to investigate the effectiveness of our prototype DOI PET system.

1. Introduction

Positron emission tomography (PET) detectors with Depth-of-Interaction (DOI) encoding capability allows high resolution and high sensitivity image to be achieved simultaneously. To measure DOI information from a mono-layer array of scintillation crystal using single-ended readout, our group has previously devised a novel method based on light spreading within a crystal^[1]. A scintillation crystal array is wrapped with triangularly teeth shaped reflector, such that scintillation photons spread simply in the y-direction in upper halves of crystal and in the x-direction in lower halves (Fig.1 (b)). As a result, DOI positions can be estimated by considering the extent of two-dimensional light dispersion. Based on both simulation and experimental studies, our proposed DOI PET detector showed promising results with high resolution and sensitivity.^[2]

While we used PMT as a photo sensor, we have extended scope of our DOI PET detector to use Silicon photomultiplier (SiPM), since SiPM has a lot of advantages such as its insensitivity to magnetic fields, high

gain, and fast timing properties. In this study, we used digital Silicon Photomultiplier (dSiPM), which has additional benefit in implementing our continuous DOI PET detector because the energy and timing information generated from each pixel of dSiPM array is digitally recorded, being available for easy estimation of light distribution. And we already presented that our DOI estimation methods is well implemented by using dSiPM as a photo sensor. It showed very good energy resolution, and also good DOI accuracy.

In this study, we developed a ring-like PET system by rotating a prototype DOI PET detector pair by using dSiPM. Monte Carlo simulation study was performed simultaneously, and the performance of our prototype DOI PET system will be evaluated.

2. Methods

2.1 DOI encoding block detector design

For each DOI detector, Philips dSiPM (DPC-3200-22-44) was optically coupled with 18×18 array of unpolished LYSO crystal ($1.47 \times 1.47 \times 15 \text{ mm}^3$) (Fig.1). Crystals were wrapped with triangular teeth shape reflector. 1 mm light guide was inserted between sensor and crystal array for efficient light spreading. Additionally, in order to reduce the effect of dead spaces between pixels of dSiPM, we used window shaped reflector placed between the sensor and light guide to reduce light loss (Fig. 1(a)).

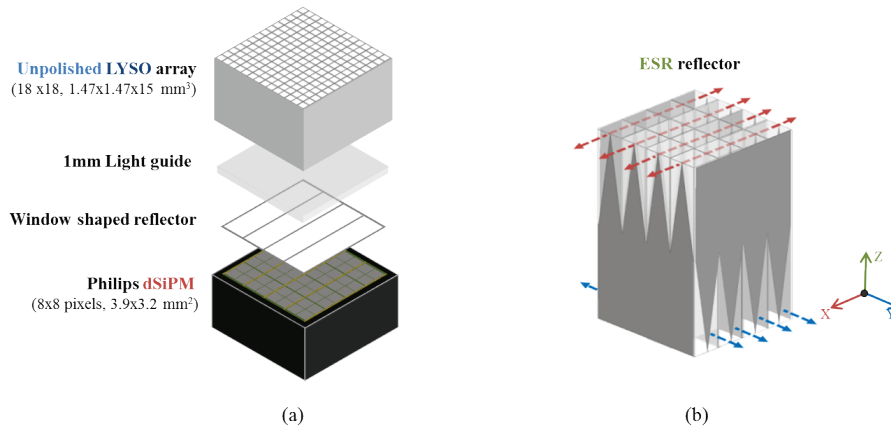


Figure 1. DOI encoding block detector design (a) detector assembly, (b) triangular teeth shape reflector.

2.2 Experiment setting and data acquisition process

In this study, the prototype DOI PET detector pair was placed on the 2-AXIS motorized rotation stage to mimic a PET ring system. We demonstrated 12-block PET ring system with crystal face-to-face distance of 12.4 cm. One detector was fixed, while the other one was rotating on AXIS-2. Source was placed on AXIS-1 and was rotating to cover all possible detector configurations of the ring geometry. (Fig. 2(a)) Data was acquired at all different detector configurations, and motions and moments of rotations were controlled automatically.

Data acquisition process was managed by using Philips Digital Photon Counting Technology Evaluation Kit (PDPC-TEK) connected to PC. Tile settings of dSiPM were configured adequately as following: trigger

scheme 4, validation scheme 8, validation length 40 ns, integration length 165 ns, and fully on neighbor logic configuration. 10% of dSiPM cells with highest dark count rate were inhibited. The whole experiment setup was placed inside the temperature controlling box set to 0°C to lower the dark count effect. (Fig. 2(b))

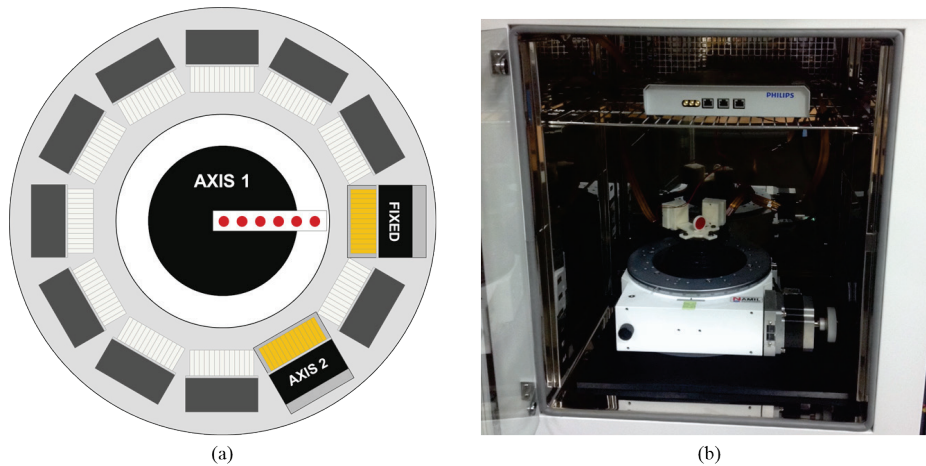


Figure 2. (a) Configurations of our prototype system, (b) experiment setting placed in the temperature controlling box

2.3 GATE simulation studies

On the other hand of experimental studies, Monte Carlo simulation studies were also performed by using GATE in order to compare results with our prototype detector pair system. In simulation studies, full-ring PET with exactly same geometry was simulated. (Fig. 3) Two different cases were simulated here: (a) PET system with no DOI information, (b) PET system with 4-region DOI information. For the latter case, number of DOI region was determined by considering our experimental results on a detector level. (IEEE 2013)

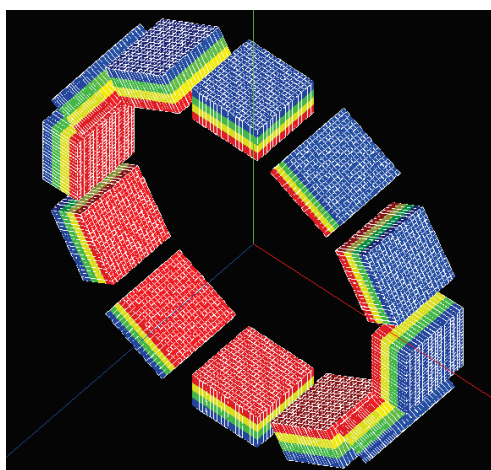


Figure 3. Full-ring PET system with 4-region DOI information

2.4 Transaxial resolution measurement study

To see the performance of our prototype DOI PET system, transaxial resolution measurement was

performed, which is the proper study to see the effect of DOI correction. Data was acquired by both experiment and simulation while moving the Na-22 point source ($12.8 \mu Ci$) in radial direction at six points starting from the center of the system with 1 cm interval (0 – 5 cm). (Fig.2 (a)) Reconstructed image will be given afterwards, and transaxial resolution of each data point will be analyzed by obtaining FWHM values. Furthermore, FWHM values will be obtain in both cases of (a) without DOI correction, and (b) with DOI correction.

3. Results and discussion

For the results, physical performances of our prototype DOI-PET detector pair will be evaluated, showing flood histogram, energy resolution, time resolution, and DOI resolution. Then the transaxial resolution (spatial resolution) along the radial direction will be evaluated from measurements while considering DOI correction. Also, there will be comparison between experiment and simulation studies.

4. Conclusions

Design of prototype DOI PET detector pair to demonstrate a ring-like PET structure is proposed and several performance tests will be performed. This prototype DOI PET system will offer high resolution and high sensitivity system which will be useful preclinical research tool.

References

- [1] M. Ito et al., “Design and simulation of a novel method for determining depth-of-interaction in a PET scintillation crystal array using a single-ended readout by a multi-anode PMT”, *Phys. Med. Biol.*, vo. 55, pp.3827-3842, July. 2010
- [2] M. Ito et al., “Continuous depth-of-interaction measurement in a single-layer pixelated crystal array using a single-ended readout” , *Phys. Med. Biol.*, vo. 58, pp.1269-1282, Feb. 2013

(5) Imaging simulation of a helmet-PET with a jaw detector

Hideaki Tashima, Hiroshi Ito and Taiga Yamaya

Molecular Imaging Center, National Institute of Radiological Sciences, Japan

Abstract

The advanced depth-of-interaction positron emission tomography (PET) detectors have been improved to provide three-dimensionally uniform detector resolution. These detectors allow geometries that place the detectors very close to imaging subjects, because they can maintain high spatial resolution even in the peripheral region in the field of view (FOV) without loss of sensitivity. In this study, we are proposing a helmet-PET geometry consisting of a hemispheric-shaped detector and a jaw detector. The key points of the geometry are the closely positioned detectors and the detector covering the jaw. The hemispheric-shaped detector had high sensitivity for the cerebrum region. However, the sensitivity at the center region was low, where the cerebellum positioned during PET measurement. In the proposed geometry, the jaw detector significantly improved the sensitivity at the center region of the geometry. High sensitivity and quantitative accuracy for the cerebellum region are important especially for functional brain imaging because this region may be used as a reference value in kinetic analysis. We conducted imaging simulations for the geometries assuming $3.0 \times 3.0 \times 3.0 \text{ mm}^3$ cubic detector elements arranged as the hemispheric-shaped detector and the jaw detector. Numerical simulations showed the proposed geometry increases image quality especially for the central region.

1. Introduction

The advanced depth-of-interaction(DOI)-PET detectors have been improved to provide three-dimensionally uniform detector resolution. We have developed the X'tal cube PET detector composed of an $18 \times 18 \times 18$ array of $1 \text{ mm} \times 1 \text{ mm} \times 1 \text{ mm}$ crystals and proven that it had isotropic spatial resolution regardless of the angle of incidence [1-3]. Another way to achieve uniform detector resolution is to stack multiple modules of 1-layer thin crystal arrays [4, 5]. The silicone photomultiplier (SiPM) enabled compact design of the PET detectors. These detectors allow a geometry that places the detectors very close to imaging subjects, because they can maintain high spatial resolution even in the peripheral region in the field-of-view (FOV) without loss of sensitivity. Dedicated brain PET scanners have been developed using DOI-PET detectors by several groups. For example, Eriksson *et al.* [6] have developed HRRT with 2-layer DOI-PET detectors. We have developed jPET-D4 with 4-layer DOI-PET detectors [7-8]. Yamamoto *et al.* [9] have developed a wearable PET system with 2-layer DOI-PET detectors. On the other hand, Majwesi *et al.* [10] have developed HelmetPET with SiPM based PET detector so that the detectors can be arranged inside a helmet to be put on a patient head. These dedicated brain PET scanners are all based on the cylinder PET geometry which is the most typical geometry for PET scanners. In this study, we are proposing a novel PET geometry that consists of a hemispheric-shaped detector and a jaw detector and is

dedicated for brain measurement (Fig. 1). It should be noted that we are expecting that a non-block-shaped detector will be developed and it will enable us to make a more flexible geometry such as this proposal in the near future. The key points of the geometry are the closely positioned detectors and the detector covering the jaw. The hemispheric-shaped geometry is expected to have high sensitivity for the cerebrum region. In addition, the jaw detector is expected to significantly improve the sensitivity at the center region of the hemisphere, where the cerebellum is positioned during PET measurement. Highly sensitive and quantitative accuracy for the cerebellum region are important especially for functional brain imaging because this region may be used as a reference value in kinetic analysis. We analyzed geometrical sensitivity for the proposed geometry.

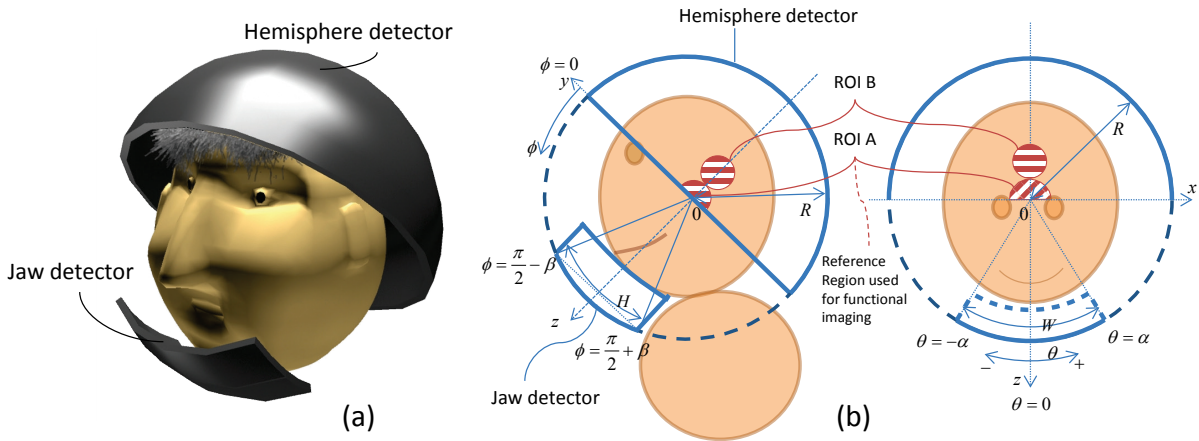


Figure 1. Conceptual illustration of the chin-strap-helmet PET consisting of a hemispheric-shaped detector and a jaw detector (a) and the parameters for determining the size of the jaw detector.

2. Methods

2.1 Helmet-PET with Jaw Detector

Our proposed geometry consists of a hemispheric-shaped detector and a jaw detector. We define the jaw detector size with two parameters α and β for the horizontal angle and vertical angle, respectively. The hemispheric-shaped detector and the jaw detector are defined on a common sphere with the radius of R . As shown in Figure 1 (b), α defines jaw detector width and β defines its height. We analyze geometrical sensitivity for each region as relative coverage of the solid angle in which the coincidence measurement is possible.

2.2 Imaging Simulation

We conducted computer simulations assuming a $3 \text{ mm} \times 3 \text{ mm} \times 3 \text{ mm}$ detector elements placed on the surface of each detector module. The detector elements were uniformly distributed on each circle with polar angle sampling on sphere. The normal vector of the detector element was matched with the normal vector of the sphere surface. The diameter of the sphere where the detector arranged was 250 mm. Figure 2 shows a numerical phantom used in the simulation. The numerical phantom was designed to have three disks and seven spots with a size of 3 mm in all directions, which corresponds a voxel. Poisson noise was added to

each line of response (LOR) bin in the projection data calculated by a forward projection and adjusted to 500 M count for fully covered geometry ($\alpha=\beta=90^\circ$). Only LOR bins where the coincidence measurement is possible with the parameters were used in the reconstruction step. We compared the helmet PET with jaw detector with a cylinder PET and helmet PET without jaw detector. The parameters for the jaw detector was $\alpha=60^\circ$ and $\beta=10^\circ$. The normalized standard deviation (NSD) was calculated for each region of interest (ROI) set inside disks as shown in figure 2.

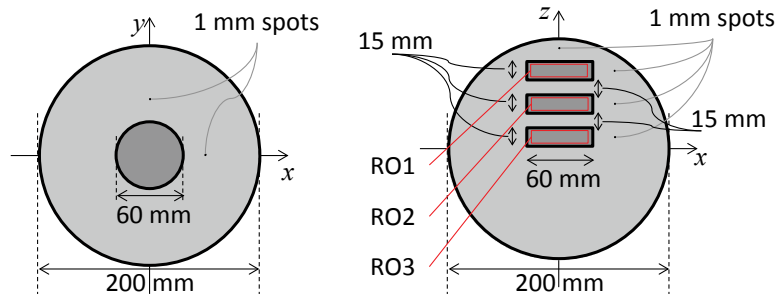


Figure 2. Numerical phantom design used for the imaging simulation.

3. Results

Figure 3 shows the geometrical sensitivity for each region calculated as relative coverage of the solid angle in which the coincidence measurement is possible. Because the sensitivity distributions were bilaterally symmetric, we combined them into one image to show the difference clearly. The sensitivity profile of the cylindrical PET having the same amount of detector surface area as the helmet PET was also plotted. The jaw detector significantly improved the sensitivity at the center region.

Figure 4 shows the images reconstructed for the each geometry. Figure 5 shows the NSD calculated for each ROI in the reconstructed images.

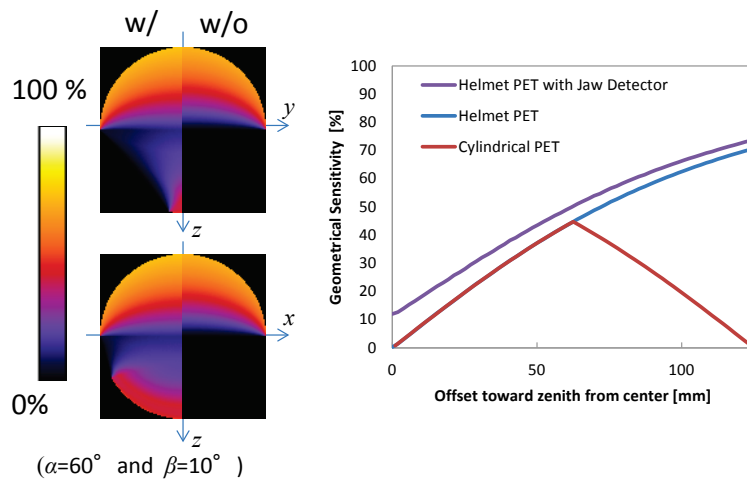


Figure 3. Sensitivity distributions of the helmet PET with and without the jaw detector (left) and its profile from the center toward zenith (right).

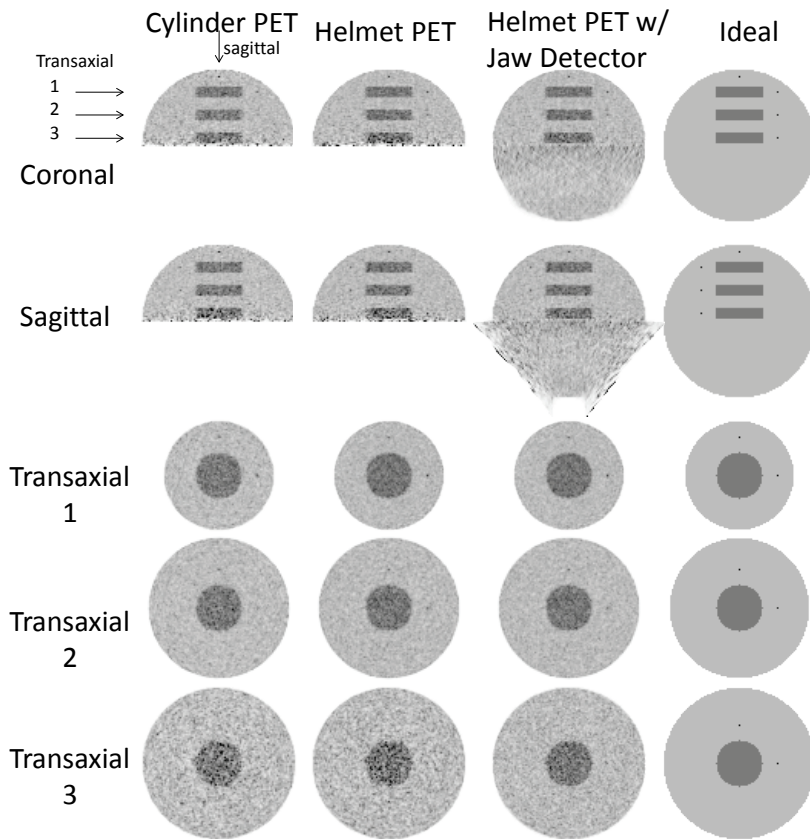


Figure 4. Reconstructed images for the cylinder PET, helmet PET, and helmet PET with jaw detector in which parameters for the jaw detector were $\alpha = 60^\circ$ and $\beta = 10^\circ$.

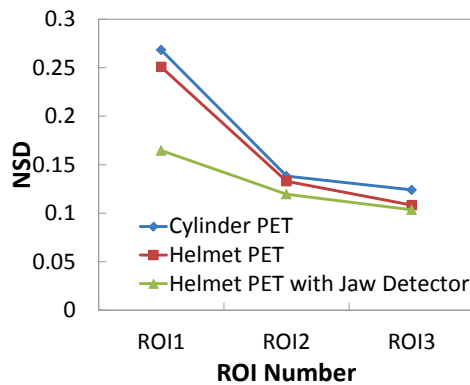


Figure 5. NSD for each ROI in the images reconstructed for the each geometry.

4. Discussion

The sensitivity for the ROI A in figure 1 (b) became 300% of that for the helmet PET and the difference between ROI A and B for the proposed geometry was decreased to only 2 times larger, which was 5 times without the jaw detector, by adding a supplemental jaw detector equivalent to only 12% of the hemispheric-shaped detector. As a result of imaging simulation, noise in the reconstructed image for the central region where corresponds cerebellum region was significantly reduced by the jaw detector.

5. Conclusions

We proposed the helmet-PET geometry having a jaw detector. Geometrical analysis and imaging simulation showed that the proposed geometry has good potential for highly sensitive and accurate measurement of brain functions.

Acknowledgments

This work was supported in part by the Japan Society of Research Fellowship for Young Scientists from the Japan Society for the Promotion of Science (JSPS).

References

- [1] T. Yamaya, T. Mitsuhashi, T. Matsumoto, et al., “A SiPM-based isotropic-3D PET detector X’tal cube with a three-dimensional array of 1 mm³ crystals,” *Phys. Med. Biol.*, 56, pp.6793-6807, 2011.
- [2] Y. Yazaki, et al., “A 3D Position-Sensitive Radiation Detector with All-Surface MPPC Readout,” *IEEE Trans. Nucl. Sci.*, vol. 59, pp. 462-8, 2012.
- [3] E. Yoshida, et al., “Intrinsic spatial resolution evaluation of the X’tal cube PET detector based on a 3D crystal block segmented by laser processing,” *Rad. Phys. Tech.*, vol. 6, pp. 21–7, Jan. 2013.
- [4] J. Zhang, et al., “Performance characterization of a novel thin position-sensitive avalanche photodiode for 1 mm resolution positron emission tomography,” *IEEE Trans. Nucl. Sci.*, vol. 54, pp. 415–421, Jun. 2007.
- [5] F. W. Y. Lau, et al., “Analog signal multiplexing for PSAPD-based PET detectors: simulation and experimental validation,” *Phys. Med. Biol.*, vol. 55, pp. 7149–74, 2010.
- [6] L. Eriksson, et al., “The ECAT HRRT: NEMA NEC evaluation of the HRRT system, the new high-resolution research tomograph,” *IEEE Trans. Nucl. Sci.*, vol. 49, pp. 2085–88, 2002.
- [7] E. Yoshida, et al., “Design and initial evaluation of a 4-layer DOI-PET system: the jPET-D4,” *Japanese Jour. Med. Phys.*, vol. 26, pp. 131–40, 2006.
- [8] T. Yamaya, et al., “Transaxial system models for jPET-D4 image reconstruction,” *Phys. Med. Biol.*, vol. 50, pp. 5339–55, 2005.
- [9] S. Yamamoto, et al., “Development of a brain PET system, PET-Hat: A wearable PET system for brain research,” *IEEE Trans. Nucl. Sci.*, vol. 58, pp. 668–673, 2011.
- [10] S. Majewski, et al., “HelmetPET: A silicon photomultiplier based wearable brain imager,” *IEEE NSS&MIC Conf. Rec.*, pp. 4030-4034, 2011.

(6) Noninvasive linear methods for human [¹¹C]ABP688 PET

Seongho Seo¹, Yu Kyeong Kim¹, Jee-Young Lee², Su Jin Kim¹, Beom S. Jeon², Dong Soo Lee¹, and Jae Sung Lee¹

¹Department of Nuclear Medicine, College of Medicine, Seoul National University, Seoul, South Korea

²Department of Neurology, College of Medicine, Seoul National University, Seoul, South Korea

Abstract

In this study, we have assessed a variety of linear methods avoiding arterial blood sampling to quantify metabotropic glutamate receptor 5 bindings from [¹¹C]ABP688 human brain PET data. All the methods showed very similar results with nonlinear simplified reference tissue model in regional analysis while only two methods among them, the relative equilibrium based graphical plot and the mixed LS-TLS based method, successfully produced good parametric images without suffering from noise or relative underestimation issues.

1. Introduction

Metabotropic glutamate receptor 5 (mGluR5) is known as a potential therapeutic target due to its involvement in various brain diseases^[1]. Although [¹¹C]ABP688 is a highly selective and promising radioligand for the mGluR5, the kinetic analysis studies for this tracer in human brain are limited to the compartment modeling and the Logan plot using plasma input function^[2-3]. Thus, we investigated the feasibility of various noninvasive linear methods using reference tissue for human [¹¹C]ABP688 PET data, focusing on the compatibility with the nonlinear simplified reference tissue model (SRTM)^[4] and quality of parametric image of the distribution volume ratio (DVR).

2. Methods

2.1 Data acquisition and processing

Total 30 subjects, including 9 controls and 21 Parkinson's disease patients, underwent a 60-min dynamic [¹¹C]ABP688 PET and T1-weighted MRI scans simultaneously using 3T Siemens Biograph mMR. For each subject, about 370 MBq (10.0 mCi) [¹¹C]ABP688 was administrated with an intravenous bolus injection, and then the emission data were acquired in list-mode. After routine corrections, 44 dynamic frames (8 × 15, 16 × 30, 10 × 60, 10 frames × 240 sec) were reconstructed by the filtered back projection. Regions-of-interest (ROIs) of putamen, caudate nucleus, hippocampus, thalamus, and cerebellum were automatically segmented from the individual MR image using the FMRIB Integrated Registration and Segmentation Tool (FIRST, FSL v4.0, Oxford University, Oxford UK, <http://www.fmrib.ox.ac.uk/fsl>). By directly placing those ROIs on the reconstructed PET images without co-registration, we obtained regional time-activity curves (TACs).

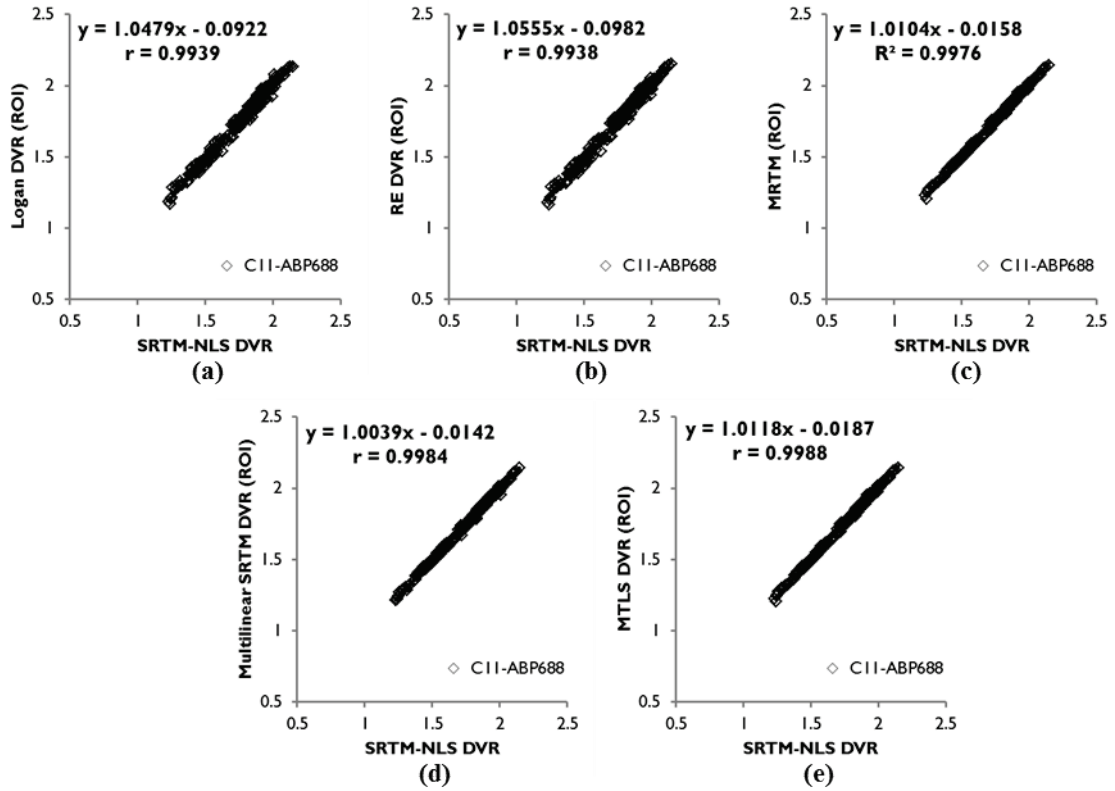


Figure 1. Linear relationship between the distribution volume ratio (DVR) estimates obtained by the standard simplified reference tissue model using nonlinear least squares (SRTM-NLS) and those by various linear methods using a reference region (the cerebellum in this study): (a) Logan plot, (b) relative equilibrium based graphical plot (RE plot), (c) multilinear reference tissue model (MRTM), (d) multilinear version of SRTM using ordinary least squares (multilinear SRTM), and (e) multilinear SRTM using the mixed LS-TLS (MTLS). Each method was applied to the region-of-interest (ROI) TACs from dynamic [^{11}C]ABP688 human brain PET data.

2.2 Quantification

For regional and voxel TACs of each subject, the DVRs were estimated from 5 different noninvasive methods using the cerebellum as a reference region. For ROI data, we compared: Logan plot^[5], relative equilibrium based graphical plot (RE plot)^[6], multilinear reference tissue model (MRTM)^[7], multilinear version of SRTM^[8] using ordinary least squares (multilinear SRTM), and the multilinear SRTM using the mixed LS-TLS (MTLS). For voxel data, MRTM and MTLS were replaced with MRTM2 and a new regularization approach for MTLS with spatial constraint (MTLS-SC) respectively because both MRTM and MTLS suffered from high spatial variability in parametric images. Results from each method were compared with those from ROI-based nonlinear SRTM (SRTM-NLS).

For the Logan plot, we ignored the term of the tissue-to-plasma efflux rate constant in a reference region ($k_{2,\text{REF}}$) or its population average ($\bar{k}_{2,\text{REF}}$) that is involved in the operational equation relying on a reference tissue input (see Discussion). For the Logan and RE plot, we determined the starting time of linear portion

t^* as 20-min post-injection by observing both graphical plots. Conversely, whole data points were used for the other three methods that are based on multiple linear regression models. On the other hand, since MRTM2 requires a priori information of $k_{2,REF}$ to reduce the number of model parameters in MRTM, we calculated it from the results of SRTM-NLS.

For MTLs and MTLs-SC, we assumed that only one independent variable (the tissue concentration) among total three independent variables of the multilinear SRTM is contaminated with noise. For MTLs-SC, we formulated and solved the following regularization problem for $\mathbf{y} = X\boldsymbol{\beta}$, a matrix form representation of the multilinear SRTM,

$$\min_{\boldsymbol{\beta}} \frac{\|X\boldsymbol{\beta} - \mathbf{y}\|_2^2}{1 + \|P\boldsymbol{\beta}\|_2^2} + \lambda \|L(\boldsymbol{\beta} - \boldsymbol{\beta}_s)\|_2^2,$$

where $\boldsymbol{\beta}$ is a vector of model parameters including DVR, $\boldsymbol{\beta}_s$ is a spatial constraint that restricts the range of bias allowed in the final solution, λ is a regularization parameter to control the balance between the MTLs cost function and the penalty (or the balance between bias and variance), L is a diagonal matrix that assigns different weights to each component of $\boldsymbol{\beta}$. In addition, $P = \text{diag}(0,0,1)$ in which the value of 1 corresponds to the noisy independent variable (the tissue concentration). The spatial constraint is generated by applying a spatial smoothing filter to the initial DVR images pre-estimated with MTLs. The penalty (the second term) in the above equation spatially constrains the resulting parameters to be around the values of neighboring voxels.

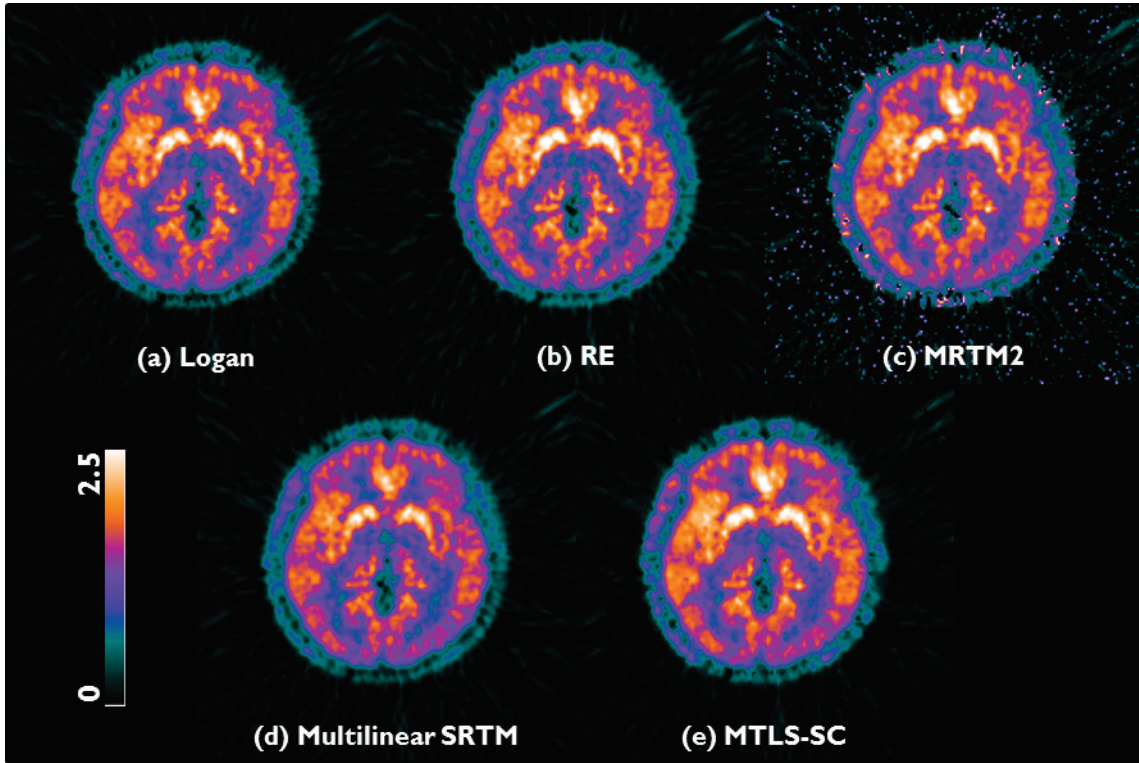


Figure 2. Transverse planes of representative parametric images of DVR acquired using various methods from $[^{11}\text{C}]\text{ABP688}$ PET data. (a) Logan plot, (b) RE plot, (c) MRTM2, (d) multilinear SRTM, and (e) MTLs-SC.

3. Results

As shown in Figure 1, the ROI DVRs from each method were almost identical to those from nonlinear SRTM ($y = 1.06x + 0.10$, $r = 0.99$ in the worst case). However, in voxelwise quantification, only the DVR parametric images from RE plot and MTL-SC showed good quality and relatively accurate regional values (RE, $y = 1.06x + 0.10$, $r = 0.99$; MTL-SC, $y = 1.02x - 0.03$, $r = 1.00$); other images suffered from influence of high-level noise in voxel TACs: decreases in DVR value or in correlation with nonlinear SRTM results (Logan, $y = 0.92x + 0.09$, $r = 0.99$; MRTM, $y = 0.97x + 0.08$, $r = 0.97$; multilinear SRTM, $y = 0.78x + 0.29$, $r = 0.97$) (Figures 2 and 3).

4. Discussion

In this study, we applied the Logan plot without the $k_{2,REF}$ term because the term can be ignored when it is relatively small or becomes constant^[5]. In fact, the use of pre-estimated values from SRTM-NLS, as in MRTM2, made negligible changes on the DVR values (not shown), and furthermore the Logan plot without the term yielded good results in ROI analysis (Figure 1).

Meanwhile, the Logan plot and the multilinear SRTM generated the parametric images with relatively lower intensities than the others (Figures 2 and 3). Those underestimations are due to the violation of the basis assumption underlying ordinary least squares: all independent variables in a given linear model are measured without noise or exactly known. Conversely, the other methods demonstrated relatively accurate results by avoiding such violation; the RE plot and MRTM (also MRTM2) use noisy data only for dependent variable and MTL-SC allows an involvement of noisy independent variables during estimation process. Nevertheless, MRTM2 produced outliers in a low binding region such as thalamus probably because the DVR is calculated by a division of the estimated model parameters, not directly estimated as in the other four methods.

Although we used the results from SRTM-NLS as a gold standard in this study, even those results may be underestimated because the human cerebellum is known to have the mGluR5 receptors^[2-3]. However, several animal studies^[9-11] have reported that the results from the noninvasive Logan and the SRTM-NLS were highly correlated with those from compartment modeling despite a slight underestimation that is attributable to specific bindings in the cerebellum. On the other hand, cerebellar gray matter has shown to be better reference region for baboon studies than the whole cerebellum^[11] and thus was also used in human study by the same group^[12]. However, in this study, we observed no difference between the results obtained using cerebellar gray matter and whole cerebellum (not shown).

5. Conclusions

For the quantification of human [¹¹C]ABP688 PET data using reference input function, RE plot and MTL-SC-based methods provided the best results in terms of the parametric image quality and the compatibility with SRTM-NLS.

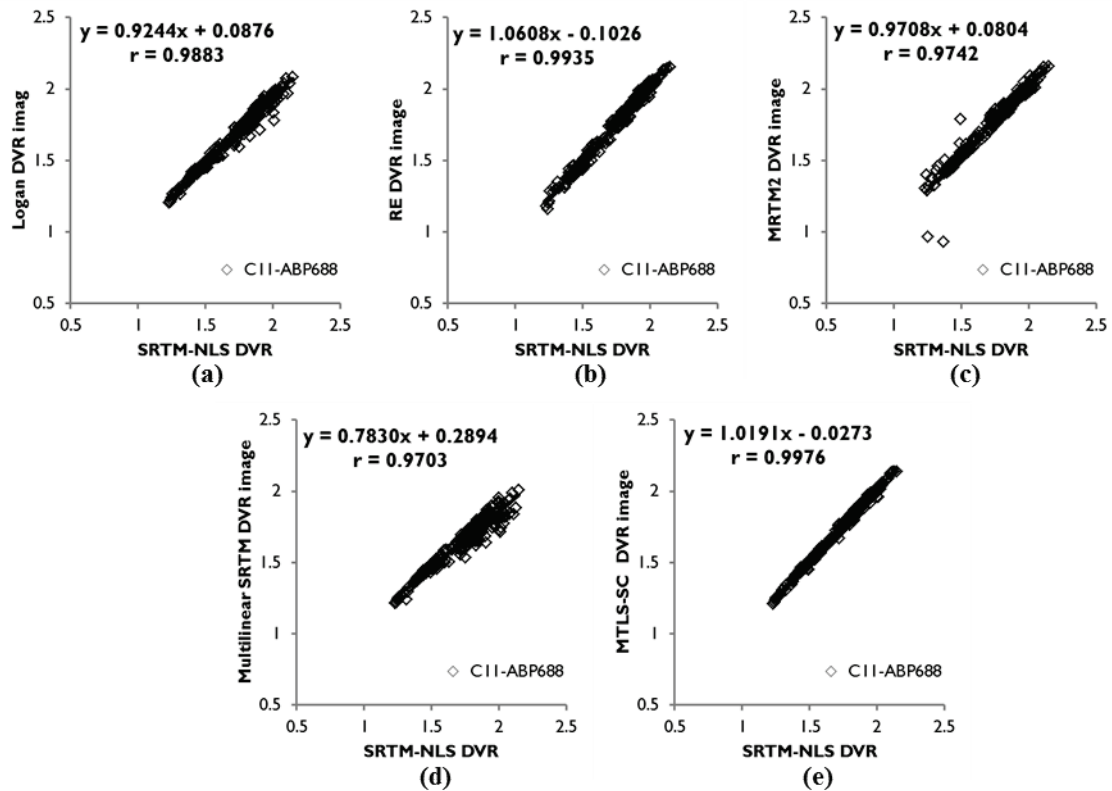


Figure 3. Linear relationship between regional mean values of DVR images from various methods and corresponding ROI DVRs from nonlinear SRTM (SRTM-NLS). Each panel corresponds to DVR image in Figure 2: (a) Logan plot, (b) RE plot, (c) MRTM2, (d) multilinear SRTM, and (e) MTLs-SC.

References

- [1] Ametamey SM, Treyer V, Streffer J, et al. Human PET studies of metabotropic glutamate receptor subtype 5 with 11C-ABP688. *J Nucl Med.* 2007;48:247–252.
- [2] Treyer V, Streffer J, Wyss MT, et al. Evaluation of the metabotropic glutamate receptor subtype 5 using PET and 11C-ABP688: assessment of methods. *J Nucl Med.* 2007;48:1207–1215.
- [3] Kågedal M, Cselényi Z, Nyberg S, et al. A positron emission tomography study in healthy volunteers to estimate mGluR5 receptor occupancy of AZD2066 - Estimating occupancy in the absence of a reference region. *NeuroImage.* 2013;82:160–169.
- [4] Lammertsma AA, Hume SP. Simplified reference tissue model for PET receptor studies. *NeuroImage.* 1996;4:153–158.
- [5] Logan J, Fowler JS, Volkow ND, Wang G-J, Ding YS, Alexoff DL. Distribution volume ratios without blood sampling from graphical analysis of PET data. *J Cereb Blood Flow Metab.* 1996;16(5):834–840.
- [6] Zhou Y, Ye W, Brašić JR, et al. A consistent and efficient graphical analysis method to improve the quantification of reversible tracer binding in radioligand receptor dynamic PET studies. *NeuroImage.* 2009;44:661–670.

- [7] Ichise M, Liow JS, Lu JQ, et al. Linearized reference tissue parametric imaging methods: application to [¹¹C]DASB positron emission tomography studies of the serotonin transporter in human brain. *J Cereb Blood Flow Metab.* 2003;23:1096–1112.
- [8] Zhou Y, Endres C, Brašić JR, et al. Linear regression with spatial constraint to generate parametric images of ligand-receptor dynamic PET studies with a simplified reference tissue model. *NeuroImage.* 2003;18:975–989.
- [9] Elmenhorst D, Minuzzi L, Aliaga A, et al. In vivo and in vitro validation of reference tissue models for the mGluR(5) ligand [(11)C]ABP688
- [10] Elmenhorst D, Aliaga A, Bauer A, et al. Test-retest stability of cerebral mGluR(5) quantification using [(11)C]ABP688 and positron emission tomography in rats. *Synapse.* 2012;66:552–560.
- [11] DeLorenzo C, Mathew SM, Brennan, K, et al. In vivo positron emission tomography imaging with [¹¹C] ABP688: binding variability and specificity for the metabotropic glutamate receptor subtype 5 in baboons. *Eur J Nucl Med Mol Imaging.* 2011;38:1083–1094.
- [12] DeLorenzo C, JSD Kumar, JJ Mann, et al. In vivo variation in metabotropic glutamate receptor subtype 5 binding using positron emission tomography and [¹¹C]ABP688. *J Cereb Blood Flow Metab.* 2011;31:2169–2180.

(7) Unconventional imaging in ion beam therapy: status and perspectives

Katia Parodi^{1,2}

¹Ludwig Maximilians University, Germany

²Heidelberg University Clinic, Germany

Abstract

The physical properties of ion beams can offer unprecedented ballistic accuracy for highly conformal irradiation of the tumour volume, with excellent sparing of surrounding healthy tissue and critical organs. However, the advantageous dosimetric properties come at the price of increased sensitivity to uncertainties in treatment planning and delivery. This calls for an increasing role of imaging to ensure safe application of the intended dose to the targeted area during the entire course of fractionated therapy. Although it is common perception that image-guidance of particle therapy lags behind modern photon therapy, new technological developments are being pursued by several groups to exploit unique features of ion beam interaction in matter for innovative and unconventional image-guidance concepts.

1. Introduction

The favourable physical and radiobiological properties of light ion beams (i.e., protons and heavier ions up to charge $Z \approx 10$) offer the possibility of a highly precise and biologically effective radiation therapy, owing to the selective concentration of radiation damage in the characteristic Bragg-peak at the end of range [1,2]. This promises improved clinical outcome with reduced toxicity for various tumour sites in comparison to conventional radiotherapy with photons and electrons. However, the increased physical selectivity of ion beam therapy comes at the price of enhanced sensitivity to inter- and intra-fractional changes of the treatment situation with respect to the planned one. In particular, the finite beam range in tissue is strongly influenced by the radiological pathlength, directly affecting the localisation of the intended dose delivery. Therefore, full clinical exploitation of the therapeutic benefits of ion beams requires imaging techniques capable of assessing the patient position and anatomy at the treatment site, as well as the actual beam range and, ultimately, the delivered dose to the patient. To this aim, several unconventional imaging modalities are being investigated to provide dedicated on-site image-guidance in particle therapy.

2. Material and methods

Reported clinical experience has been so far restricted to the in-vivo visualization of beam range via Positron-Emission-Tomography (PET) and Magnetic Resonance Imaging (MRI), mostly after individual or cumulated treatment fractions, respectively [3]. The former technique exploits the transient amount of β^+ -activation induced in nuclear reactions between the primary beam and the irradiated tissue, thus depending on the ion beam species, the elemental composition and physiological (in terms of biological clearance or so-called “washout”) properties of the irradiated tissue, as well as the time course of irradiation

and data acquisition. The latter modality exploits the detectability in MR images of radiation-induced physiological changes, which can manifest after a certain dose threshold in particular anatomical locations such as the spine and the liver. For on-site imaging directly during the beam delivery, new detector developments aim at in-vivo range verification via visualization of secondary emerging radiation either from delayed radioactive decays of β^+ -activated isotopes (PET imaging) or from prompt de-excitation products of nuclear fragmentation reactions (prompt gamma and charged particle imaging). All these (quasi) real-time techniques could be complemented by radiographic or tomographic transmission imaging of energetic ion beams prior to, or even “in-between”, treatment in order to (i) decrease range errors via direct determination of the tissue stopping properties relative to water (owing to their weak dependence on the beam energy), (ii) provide imaging of the patient with reduced artefacts from metal/dental implants and, ultimately, (iii) replace in-room X-ray imaging for daily low-dose image guidance and, if necessary, treatment adaptation.

3. Results

Following the encouraging results from the clinical usage of often suboptimal instrumentation and implementation of PET-based treatment verification, promising new detector concepts and imaging prototypes for on-site image-guidance have been proposed and demonstrated in proof-of-principle experiments by several groups. Whereas next-generation dedicated PET instrumentation essentially relies on full-ring (“openPET” [5]) or dual-head (with ultra-fast time-of-flight [6]) designs for in-beam imaging, different concepts have been proposed for the detection of neutral or charged prompt secondary radiation from nuclear interactions in the patient. Prototypes for prompt gamma imaging perpendicular to the main beam direction span from one-dimensional visualization of the last few centimeters of beam penetration through a massive knife-edge collimator [6] to the more challenging three-dimensional detection relying on Compton kinematics [7]. Imaging of charged particles (essentially protons) was demonstrated with tracking systems inspired by particle physics experiments, using solid state detectors or drift chambers followed by absorbers, placed at different angles from the main beam direction [8,9]. Finally, recent implementations of ion transmission imaging include particle-by-particle tracking with residual energy measurement for broad beams, and range assessment from transmission measurements in planar detectors or Bragg peak visualization in so-called range telescopes for pencil-like beams [10].

4. Discussion and conclusions

The rapidly increasing spread of particle therapy facilities is being accompanied by an increasing role of unconventional imaging modalities aiming to reduce range and dose delivery uncertainties for optimal clinical usage of ion beams. Whereas a limited number of clinical investigations have been so far reported for PET- and MRI-based range assessment after individual or cumulated treatment fractions, several groups worldwide are pioneering new detector developments aiming to (quasi) real-time on-site imaging of radioactive or prompt nuclear reaction products, possibly complemented by morphological imaging with the same radiation quality but higher energy as for therapy. Although most of the new developments are

still at the research and development level, it is expected that some of these new concepts will be deployed for clinical usage in the near future. From the different nature of the underlying signal, it can be argued that the novel imaging modalities will often provide complementary information, and their performance will be likely dependent on the ion species and anatomical site. On the other hand, even when neglecting cost issues, it could be challenging and even unpractical to integrate all the discussed techniques at the treatment site (figure 1). Therefore, hybrid detector concepts [11] serving for multiple detection purposes at the likely expense of image quality compromises might be a viable solution for the future. Additional challenges will include the synchronization of the new detector developments with motion monitoring sensors for anatomical locations subject, for example, to respiratory motion.

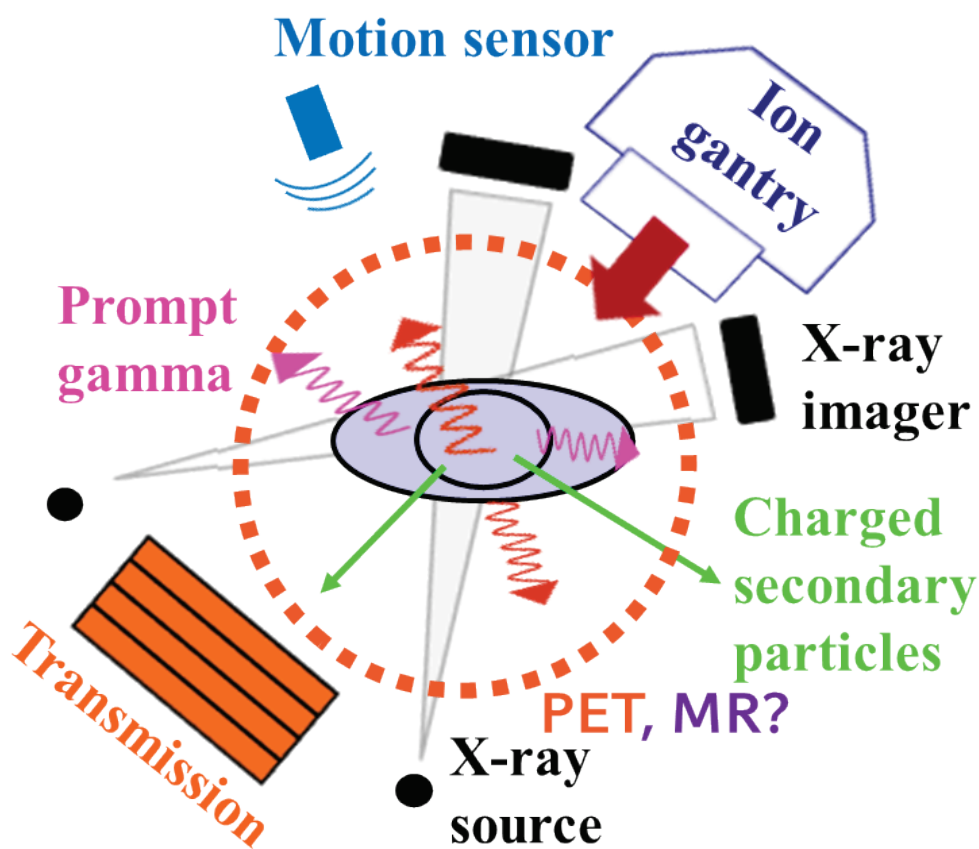


Figure 1. Schematic view of discussed imaging techniques which could complement the currently available X-ray radiographic systems for unconventional image-guidance in ion beam therapy

Acknowledgments

The author acknowledges funding from the German Research Foundation (DFG) on two projects aiming at the development of detector prototypes for ion radiography/tomography and prompt gamma imaging. Participation to the workshop was supported by the Japan Society for the Promotion of Science (fellowship S 13062).

References

- [1] R.R. Wilson, "Radiological use of fast protons". *Radiology*. 47, 1946
- [2] M. Durante and J. Loeffler, "Charged particles in radiation oncology". *Nat. Rev. Clin. Oncol.* 7, 2010
- [3] A.C. Knopf and A. Lomax, "In vivo proton range verification: a review", *Phys. Med. Biol.* 58, 2013
- [4] H. Tashima, T. Yamaya, E. Yoshida, S. Kinouchi, M. Watanabe and E. Tanaka, "A single-ring OpenPET enabling PET imaging during radiotherapy", *Phys. Med. Biol.* 57, 2012
- [5] P. Crespo, G. Shakirin, F. Fiedler, W. Enghardt and A. Wagner, "Direct time-of-flight for quantitative, real-time in-beam PET: a concept and feasibility study", *Phys. Med. Biol.* 52, 2007
- [6] V. Bom, L. Joulaeizadeh and F. Beekman, "Real-time prompt γ monitoring in spot-scanning proton therapy using imaging through a knife-edge-shaped slit", *Phys. Med. Biol.* 57, 2012
- [7] F. Roellinghoff, M.-H. Richard, et al, "Design of a Compton camera for 3D prompt- γ imaging during ion beam therapy", *Nucl. Instrum. Meth. A* 648, Suppl. 1, 2011,
- [8] C. Agodi, G. Battistoni et al, "Charged particle's flux measurement from PMMA irradiated by 80 MeV/u carbon ion beam." *Phys. Med. Biol.* 57, 2012
- [9] K. Gwosch, B. Hartmann, J. Jakubek, C. Granja, P. Soukup, O. Jäkel, M. Martišíková. "Non-invasive monitoring of therapeutic carbon ion beams in a homogeneous phantom by tracking of secondary ions." *Phys Med Biol.* 58, 2013
- [10] K. Parodi, "Heavy ion radiography and tomography", *Phys. Med.*, in press (2014)
- [11] C. Lang, D. Habs, K. Parodi and P.G. Thirolf, "Sub-millimeter nuclear medical imaging with high sensitivity in positron emission tomography using $\beta^+\gamma$ coincidences", *J. Instrum.* 9, 2014

(8) Intraoperative molecular imaging probes

Seong Jong Hong^{1,2}, Gun Chul Hong^{1,3}, In Suk Kwak^{1,3}, Hyung Seok Lee¹, Han Gyoo Kang¹,
Jeong-Whan Son⁴, Jae Sung Lee⁴, Kyeong Min Kim⁵ and Ho-Young Lee⁴

¹ Department of Radiological Science, Eulji University, Korea

² Department of Senior Healthcare (BK21 plus), Graduate School, Eulji University, Korea

³ Department of Nuclear Medicine, Samsung Medical Center, Korea

⁴ Department of Nuclear Medicine, Seoul Nat'l University College of Medicine, Korea

⁵ Korea Institute of Radiological and Medical Science, Korea

Abstract

Three different types of intraoperative molecular imaging cameras are being investigated. The first type detects electrons and gammas from ^{18}F FDG with a Hamamatsu MPPC, and the second counts Cerenkov photons, electrons and gammas from ^{18}F FDG with a CCD camera. The last one detects 140 keV gammas from $^{99\text{m}}\text{Tc}$ and near infrared (NIR) photons from indocyanine green (ICG) for sentinel lymph node identification with CCD cameras. Preliminary results are reported using an IVIS Spectrum instead of CCDs.

1. Introduction

Intraoperative molecular imaging probes are being widely used for sentinel lymph node identification and residual tumor removal by detecting electrons and/or gammas from ^{125}I , ^{111}In and $^{99\text{m}}\text{Tc}$. Recently, intraoperative probes for ^{18}F FDG have been developed since positron emission tomography (PET) became an important imaging tool for tumor detection and staging^[1]. Intraoperative imaging probes detecting Cerenkov photons from ^{18}F FDG have been also investigated^[2]. Intraoperative probes detecting electrons or positrons have a high tumor background ratio with limited in-depth detection capability while those detecting gammas usually have a low tumor background ratio. Several groups developed intraoperative probes which detect electrons (or positrons) and gammas. Lately, intraoperative NIR cameras are also being used for sentinel lymph node identification^[3].

In this paper, we report investigative researches on three different types of intraoperative cameras. The structure of the first type is presented along with the depth of interaction (DOI) capability for electron interaction point identification. A preliminary design of the second type is shown with the measured counts of Cerenkov photons, electrons and gammas from ^{18}F FDG. Finally, the measured counts of gammas from $^{99\text{m}}\text{Tc}$ and NIR photons from ICG using an IVIS Spectrum are presented with a possible scheme of simultaneous gamma and NIR photon detection.

2. Methods

2.1 Electron/Gamma Camera

The electron/gamma camera that we are investigating provides a tumor image by detecting electrons (or positrons) from superficial tumors with a gamma detection capability which compensates limited in-depth penetration of electrons. The electron/gamma camera shown in Figure 1 consisted of 4 polished plastic scintillators of $2.0 \times 2.9 \times 12 \text{ mm}^3$, a $9.0 \times 12.0 \times 12.0 \text{ mm}^3$ GAGG scintillation crystal and an MPPC readout. The front plastic and back GAGG scintillators detect electrons and gammas, respectively. The front plastic scintillators were wrapped with laser-processed multi-holes 3 M ESR polymers shown in Figure 1(c). Since more lights move to neighbor cells as the interaction point moves away from the MPPC as shown in Figure 1(d), the vertical position can be estimated by the degree of light spreads. ^{18}F FDG was used to investigate the properties of the electron/gamma camera.

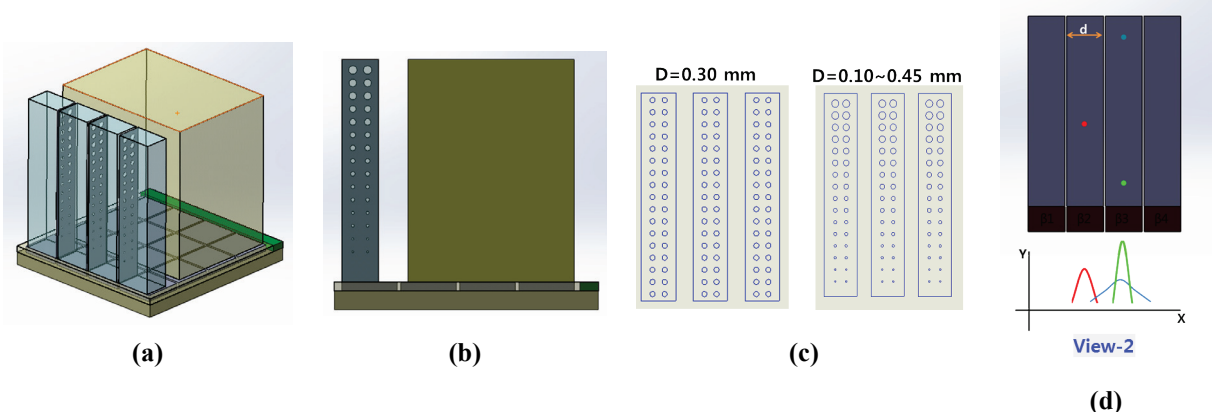


Figure 1. (a) Schematic of electron/gamma camera, (b) Front plastic scintillator and back GAGG scintillation crystal block, (c) Laser-processed multi-holes 3 M ESR polymers, (d) Schematic of light spreads depending on the vertical interaction point.

2.2 Cerenkov/Electron/Gamma Camera

The Cerenkov/electron/gamma camera aims to detect Cerenkov photons, electrons and gammas using an optical imaging system such as IVIS Spectrum. Figure 2 shows a schematic of the Cerenkov/electron/gamma intraoperative imaging camera which consists of UV fibers for Cerenkov photon passage, 0.5 mm thick GAGG scintillation crystal/clear fibers for beta detection and scintillation photon passage, and 5.0 mm thick GAGG scintillation crystal/clear fibers for gamma detection and scintillation photon passage. Figure 3 shows a test setup.

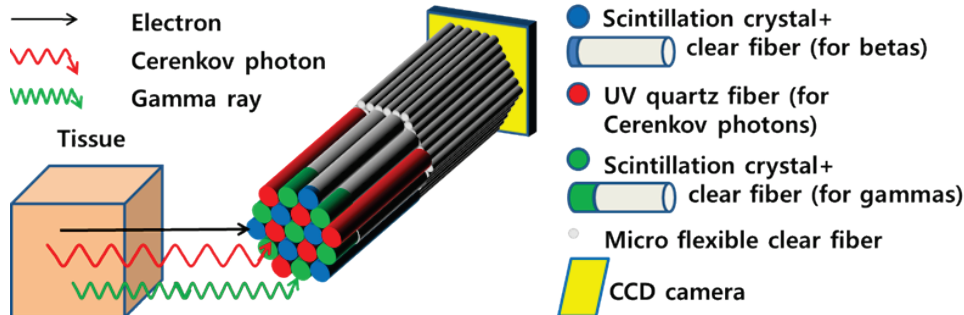


Figure 2. Schematic of electron/gamma camera.

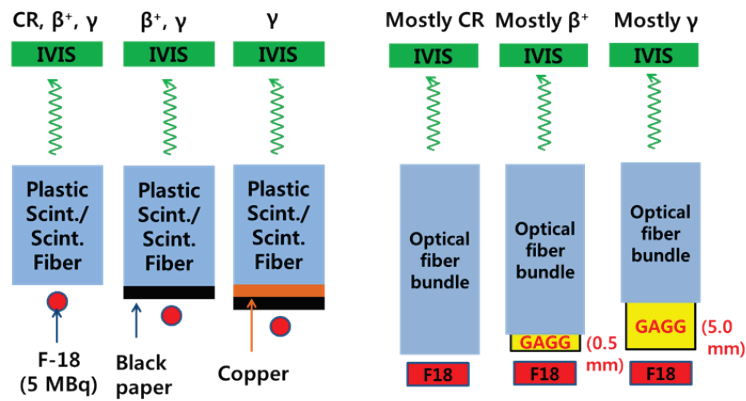


Figure 3. Test setup to measure the counts of Cerenkov photons, positrons and gammas from ^{18}F FDG.

2.3 Gamma/NIR Camera

To investigate feasibility of the simultaneous gamma and NIR camera for sentinel lymph node identification, we measured the counts of gammas from $^{99\text{m}}\text{Tc}$ and NIR photons from ICG using an IVIS Spectrum, as shown in Figure 4.

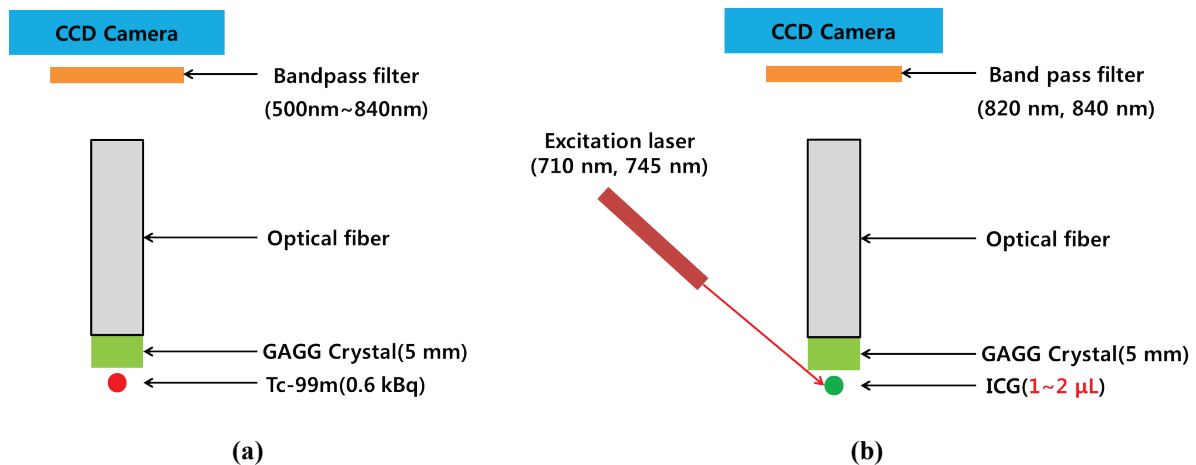


Figure 4. (a) Test setup for the detection of gammas from $^{99\text{m}}\text{Tc}$ which interacts with the GAGG crystal to generate scintillation photons. (b) Test setup for the detection of NIR photons from ICG. The GAGG crystal doesn't play a specific role other than an NIR photon conduit.

3. Results

3.1 Electron/Gamma Camera

Figure 5(a) shows hole positions on a 0.2 mm thick copper sheet to block positrons other than at 1 mm diameter holes. The DoI ratios shown in Figure 5(b) are defined by the ADC value at A divided by the sum of ADC values at A, B, C and D. Figure 5(c) shows ADC spectra at A, B, C and D channels indicating significant gamma contamination despite of the 2 mm thick polished plastic scintillator. The gamma contamination also makes it difficult to estimate the DoI resolution for positron interaction point identification. The DoI resolution of 5.79 mm could have been improved if unpolished plastic scintillators were used.

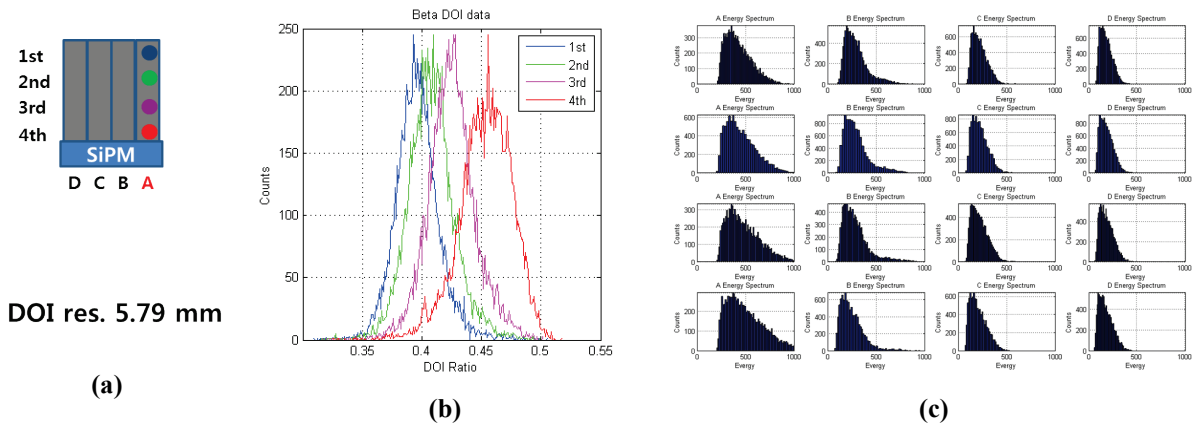


Figure 5. (a) Hole positions to allow positron and gamma passage. (b) DoI ratios depending on the hole positions. (c) ADC spectra at A, B, C and D channels. The bottom left spectrum was obtained from the 1st position at channel A.

3.2 Cerenkov/Electron/Gamma Camera

As shown in Figure 6, the plastic scintillator and scintillation fiber bundle produced a negligible intrinsic background while the GAGG scintillation crystals produced a significant intrinsic background. A relative intensity of Cerenkov photons, scintillation photons from the interaction of positrons and gammas was 1.00 : 0.15 : 1.11 with the 2.0 mm thick plastic scintillator, 1.00 : 0.22 : 0.88 with the scintillating fiber bundle, and 1.00 : 7.30 : 48.4 with the GAGG scintillation crystals.

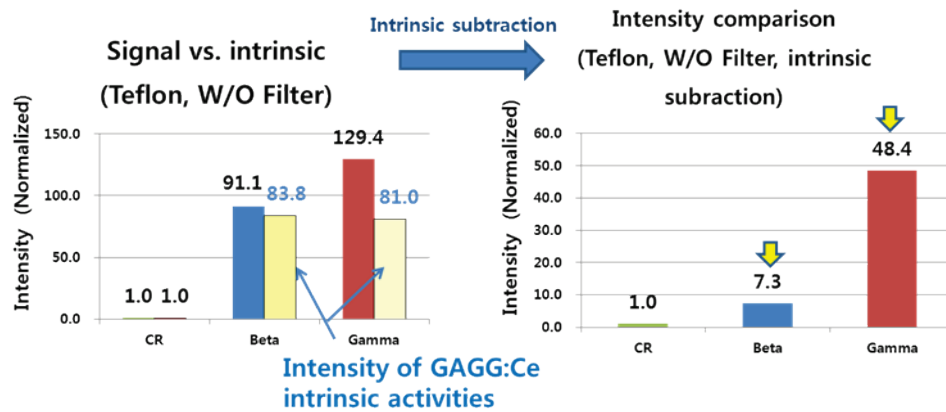


Figure 6. Signal and background counts for Cerenkov, positron and gamma measurements.

3.3 Gamma/NIR Camera

Figure 7(a) shows a characteristic spectrum of GAGG scintillation photons with a total 5.5 M counts for 10 sec. ICG intensities depending on the excitation pulse and the band pass filter were shown in Figure 8(a).

The 710 nm excitation refers to 710 ± 10 nm, and the 820 nm band pass filter passes the NIR photons with 820 ± 10 nm.

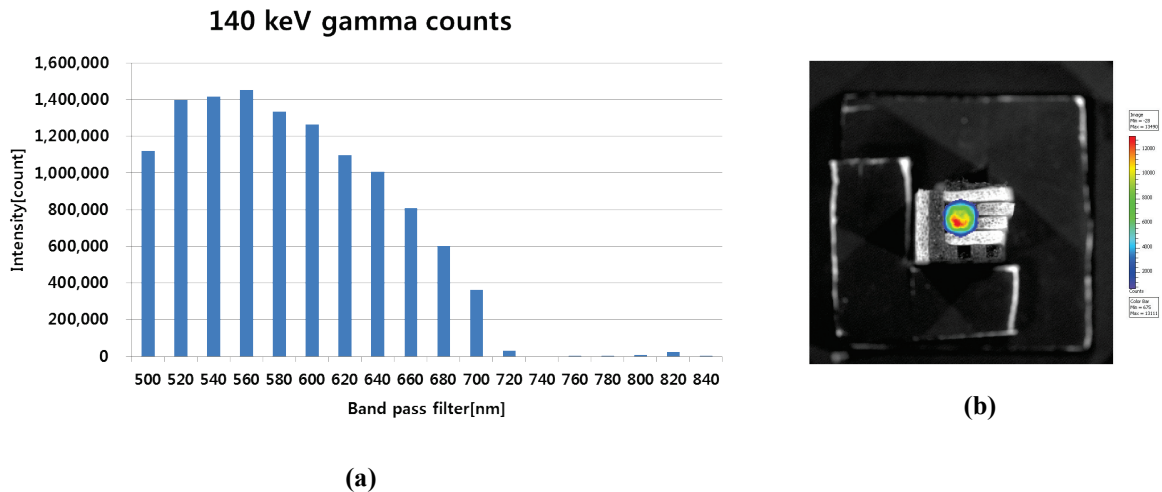


Figure 7. (a) Spectrum obtained from the GAGG scintillation crystal, (b) IVIS Spectrum image of ^{99m}Tc distribution.

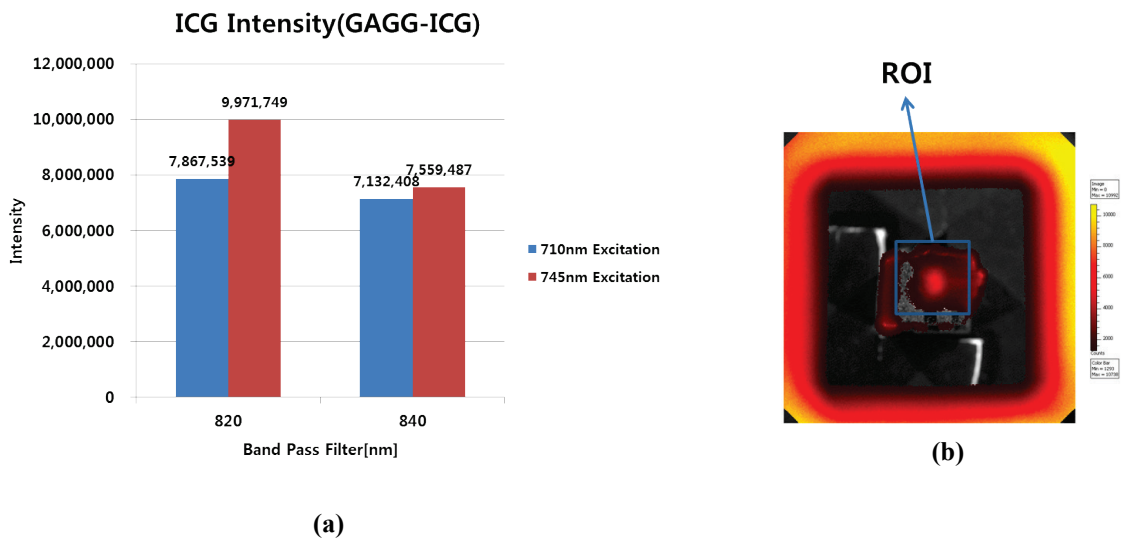


Figure 8. (a) ICG intensities depending on the excitation pulse and the band pass filter. (b) IVIS Spectrum image with region of interest (ROI) used for ICG intensity counts.

4. Discussion

The significant gamma contamination of the electron/gamma camera also makes it difficult to obtain the positron map from ^{18}F FDG. The DoI resolution of 5.79 mm was obtained with polished and cracked plastic scintillators, and it could be improved with unpolished good quality plastic scintillators. As expected for the Cerenkov/electron/gamma camera for ^{18}F FDG, the insignificant contribution of Cerenkov photons compared to positrons and gammas was obtained. Since the afterglow of GAGG was also significant, other scintillation crystals such as BGO and GSO need to be evaluated.

Significant counts from the GAGG scintillation crystal were measured using the IVIS Spectrum optical imaging system, along with the NIR photons from ICG. With these encouraging results, we propose a

simultaneous gamma/NIR photon camera shown in Figure 9 for sentinel lymph node identification. The band pass filter for scintillation photons can be chosen to maximize the acceptance of scintillation lights and to minimize the ambient lights in the operation room.

Simultaneous Gamma/Fluorescence Detection

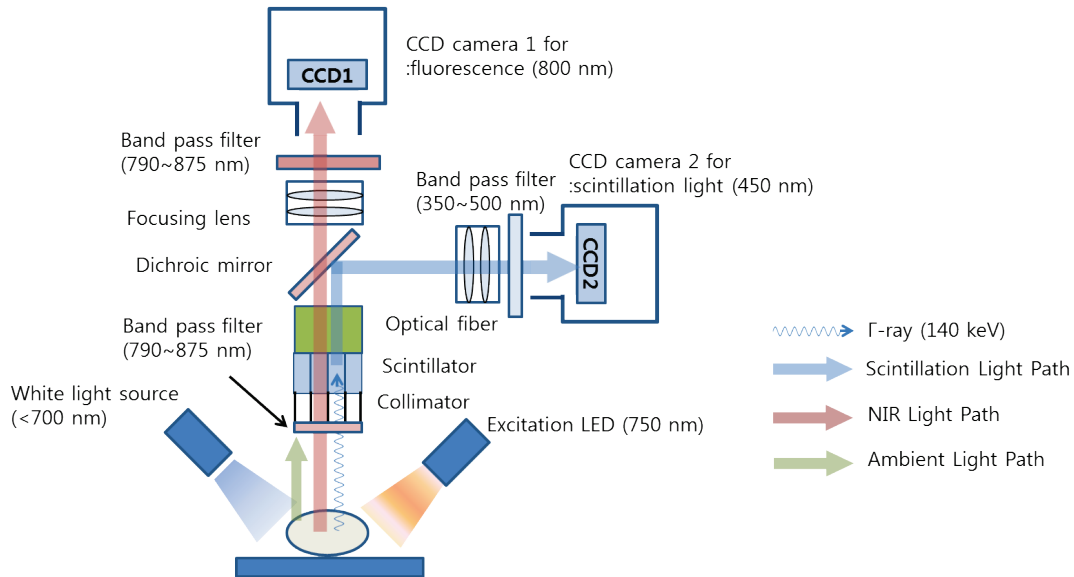


Figure 9. Layout of simultaneous gamma/NIR photon camera.

5. Conclusions

We reported investigative researches on three intraoperative molecular imaging probes. Even though lots of works are to be done, some interesting results such as the detection of scintillation photons using an optical imaging system were obtained to propose the first simultaneous gamma/NIR photon camera, to our knowledge.

Acknowledgments

The present study was supported by an Eulji University grant in 2013.

References

- [1] S. Yamamoto, et al., "An intra-operative positron probe with background rejection capability for FDG-guided surgery," *Ann. Nucl. Med.* 19(1), pp.23-28, 2005.
- [2] J. Cho, et al, "Cerenkov radiation imaging as a method for quantitative measurements of beta particles in a microfluidic chip," *Phys. Med. Biol.* 54, pp.6757-6771, 2011.
- [3] N. S. van den Berg, et al, "Sentinel Lymph Node Biopsy for Prostate Cancer A Hybrid Approach," *J. Nucl. Med.* 54, pp.493-496, 2013.

(9) Development of PET and multi-modality imaging systems based on new concepts

Seiichi Yamamoto¹

¹ Nagoya University Graduate School of Medicine, Japan

Abstract

The author proposes PET and multi-modality imaging systems based on new concepts. The PET system based on new concept is named “Split-PET” system which can be divided the detector ring into two halved rings from the center of the detector ring. With this configuration, we can easily set the PET system in the enclosed space such as neck or axilla. The Split-PET will be useful for plant research as well as in-beam experiments on proton therapy facilities. The multi-modality imaging system based on new concept is integrated PET/Cerenkov-light imaging system with which PET and Cerenkov-light images can be acquired simultaneously. This new multi-modality imaging system will be useful for the evaluation of the potential of Cerenkov-light imaging for molecular imaging.

1. Introduction

New PET and multi-modality imaging systems were developed recently and efforts to improve their performance are being continued [1-4]. Another important works for us to do is to propose new concepts for expanding and strengthening the research fields on molecular imaging instrumentation development. For this purpose, we propose PET and multi-modality imaging systems based on new concepts; they are “Split-PET” and “integrated PET/Cerenkov-light imaging” systems.

2. Methods

2.1 Split-PET

The Split-PET system has two modes. One is the split-mode in which the detector ring is separated into two parts. Thus, small part surrounded by larger parts of the subject such as neck can be positioned within the field-of-view (FOV). For in-beam PET application [5-6], proton beam can be irradiated to subject through the open space between the halved detector rings. In this mode, projection image between two halved detector rings can also be acquired. The other is the closed-mode in which the detector ring is closed to be standard circular ring to measure the reconstructed images of the subject. We developed the Split-PET system using flat panel photomultiplier tubes (FP-PMTs: Hamamatsu H8500) and dual-layer GSO block detectors. The block detectors used two types of GSO pixels (Ce: 1.5mol%: 1.6 x 2.4 x 7mm and Ce: 0.4mol%, 1.6 x 2.4 x 8mm). They are arranged into blocks of 11 x 15 matrix, and optically coupled each other to form a depth-of-interaction (DOI) block detectors. Eight block detectors are arranged in 95mm diameter ring. Mechanical system was also developed to change the split- and closed-mode.

2.2 Integrated PET/Cerenkov-light imaging system

The integrated PET/Cerenkov-light imaging system consists of a dual head PET system, mirror located

upper side of the subject and a high sensitivity charge coupled device (CCD) camera. With the system, high resolution Cerenkov-light image can be acquired [7] with the PET image. These parts are installed inside a black box because Cerenkov-light imaging requires highly dark environment. The dual head PET system employed 1.2 x 1.2 x 10mm GSO pixels arranged into 33 x 33 matrix and optically coupled to FP-PMTs (Hamamatsu: H12700) to form a GSO block detectors. Two block detectors were arranged in opposed directions with 10cm apart and a subject was positioned between the detectors. The Cerenkov-light from the upper side of the subject is reflected by the mirror, changed the direction to the side of the PET system and imaged by the high sensitivity CCD camera (Hamamatsu: ORCA II-ER).

3. Results

3.1 Split-PET

In the closed-mode, the Split-PET had spatial resolution of 2.4mm FWHM at the image center. The point source sensitivity was 1.7% at the center of the axial field-of-view (FOV). We successfully measured reconstructed phantom images acquired with the Split-PET in closed-mode. In the split-mode, similar image quality and spatial resolution were obtained in projection images.

3.2 Integrated PET/Cerenkov light imaging system

The dual head PET used for the integrated PET/Cerenkov light imaging system had spatial resolution of ~1.3mm FWHM in the projection image. The sensitivity was ~0.25% at the center of the FOV. The spatial resolution of the Cerenkov-light imaging system was excellent; it was ~200um measured with Na-22 point source less than 100um diameter. Using the combined PET/Cerenkov-light imaging system, varieties of subjects were simultaneously acquired. We could successfully obtain fused images from the simultaneously acquired images with PET and Cerenkov-light imaging.

4. Conclusions

We could develop PET and multi-modality imaging systems based on new concepts. The Split-PET is promising for many applications such as organ specific imaging and in-beam PET imaging for proton therapy. The integrated PET/Cerenkov-light imaging system will be useful to evaluate the value of Cerenkov-light imaging directly compared with PET images. Interesting information will be provided with these newly developed systems.

References

- [1] Kwon SI, et al.. J Nucl Med.;52(4):572-9, 2011
- [2] Yamaya T., et al. Phys. Med. Biol., 56, pp.6793-6807, 2011.
- [3] Yamamoto S, et al. Phys Med Biol., 7;55(19):5817-31, 2010
- [4] Yamamoto S, et al. Phys Med Biol.;57(2):N1-N13, 2011
- [5] Yamaya T, et al. Phys. Med. Biol. 56 1123–37, 2008
- [6] Tashima H, et al. Phys Med Biol.;57(14):4705-18, 2012
- [7] Robertson R, et al. Phys Med Biol. 54(16):N355-65, 2009

(10) Approach of hybrid PET imaging for improved quantification

Kyeong Min Kim¹, Byung Hyun Byun² and Sang Moo Lim^{1,2}

¹ Molecular Imaging Research Center, ² Department of Nuclear Medicine,
Korea Institute of Radiological and Medical Sciences, Korea

Abstract

It is well known that the combinational use of anatomical and functional images should be more informative and helpful to understand the physiological phenomena in clinical and preclinical studies. By virtue of success of PET/CT, the hybrid use of PET with MRI has been also expected to provide new strategy in the both fields of clinical and preclinical research. Recent development of clinically available PET/MRI system leads to increased need of new diagnostic paradigm using quantitative and functional images of PET and MRI together. In this summary, we introduce the preliminary results of quantitative evaluation using PET and MRI in clinical oncologic study of therapeutic response monitoring.

1. Introduction

The degree of FDG uptake is positively correlated with the histological grade of cancer, and FDG-PET makes it possible to assess the glucose metabolism and the metabolic activity of cancer tissue. Therefore, FDG-PET imaging has been used in tumor detection and monitoring of therapeutic response after chemotherapy. In the assessment of tumor metabolism, the standardized uptake value (SUV) is a most widely used index for quantitative evaluation, because of its simplicity in use.

Recently, the use of MR imaging has been increased in clinical oncology. In addition to conventional anatomical imaging, the functional MRI techniques are used to provide quantitative tumor imaging. Among various functional MRI techniques, the diffusion-weighted imaging (DWI) is known to show in vivo images of biologic tissues weighted with the local microstructural characteristics of water diffusion. And the apparent diffusion coefficient (ADC), which is based in DWI, can be used to measure the degree of water diffusion. Because ADC shows the tendency of decrease in highly cellular tissue such as malignant tumors, the measurement of ADC value change in tumor region after chemotherapy has been reported to be useful in monitoring therapeutic response of tumor.

In this study, the potential of combined use of FDG-PET and ADC-MRI in quantitative evaluation of therapeutic response has been examined.

2. Methods

2.1 Patients and Imaging Acquisition

Retrospective data from the both groups of patients with osteosarcoma and breast cancer have been used in this study. All patient performed repeated acquisitions of PET/CT and MRI before and after chemotherapy. The PET/CT scanner (Biograph 6; Siemens Medical Solutions) was placed parallel to the 3T

MRI scanner (MAGNETOM Trio A Tim; Siemens Medical Solutions). These 2 scanners were located 10 m apart, separated by an antimagnetic wall. PET/CT imaging was performed 60 min after FDG injection. Then, MR images covering the tumor sites were acquired immediately after the completion of PET/CT scanning. Both PET/CT and MR images were acquired with the patient supine. For patients with breast cancer, additional dedicated scans of PET/CT and MRI for breast region were performed. MR imaging included a T1- and T2-weighted sequences. Diffusion-weighted images were acquired using a spin-echo-type single-shot echo-planar imaging sequence. Imaging was performed with b values of 0 and 800 s/mm². Diffusion images were integrated in the 3 orthogonal directions to calculate the ADC maps. All patients provided written informed consent, and this study was performed according to the ethical guidelines of our institutional clinical research committee.

2.2 Image Analysis

Sequential FDG PET/CT and ADC images were automatically or manually co-registered and reviewed on the e-soft workstations (Siemens Medical Systems). An ellipsoid volume of interest including tumor was drawn and measured the SUV_{max} on each PET/CT dataset. Tumor volume based on MR images (MRV) was also calculated from the tumor length. From the PET and MRI obtained before (1) and after (2) chemotherapy, the values of SUV_{max} and ADC were measured, respectively, and calculated the differences ($\Delta\text{SUV}_{\text{max}} = \text{SUV}_{\text{max}1} - \text{SUV}_{\text{max}2}$ and $\Delta\text{ADC} = \text{ADC}_1 - \text{ADC}_2$).

We generated voxel-based maps of ΔSUV and ΔADC to support this comparison. In parametric map generation, FDG-PET and ADC-MRI images obtained before (1) and after (2) chemotherapy were co-registered, registered. Using co-registered images, subtracted images of FDG-PET (=FDG₁ - FDG₂) and ADC-MRI (=ADC₁-ADC₂) were generated. All voxel values in tumor region of subtracted images of FDG-PET and ADC-MRI were segmented into three regions of unchanged, increased, and decreased SUV or ADC values, based on the threshold of SUV or ADC changes and statistical distribution of subtracted images^[1].

3. Results

In the data of patients with osteosarcoma, after chemotherapy, both groups of good and poor responder showed good negative relationship between $\Delta\text{SUV}_{\text{max}}$ and ΔADC (Figure 1). ΔMRV showed no significant correlation between $\Delta\text{SUV}_{\text{max}}$ or ΔADC . This results mean functional parameter of FDG-PET or ADC-MRI will be more helpful, rather than the anatomical image, for accurate evaluation. Furthermore, in ROC analysis, the combined use of $\Delta\text{SUV}_{\text{max}}$ and ΔADC showed the biggest AUC and best diagnostic power in therapeutic response evaluation (Figure 2).

In quantation of ADC value, the guide of SUV_{max} to place ROI on ADC map contributes to increase significantly the correlation between ADC and SUV (Figure 3). Likewise the cases of osteosarcoma, in the data of breast cancer, the combined use of SUV and ADC provided bigger AUC value, compared to SUV only or ADC only, in ROC analysis (Figure 4).

Both maps of statistically normalized ΔSUV and ΔADC could be generated by our strategy and provided

parametric image showing tumor response (Figure 5).

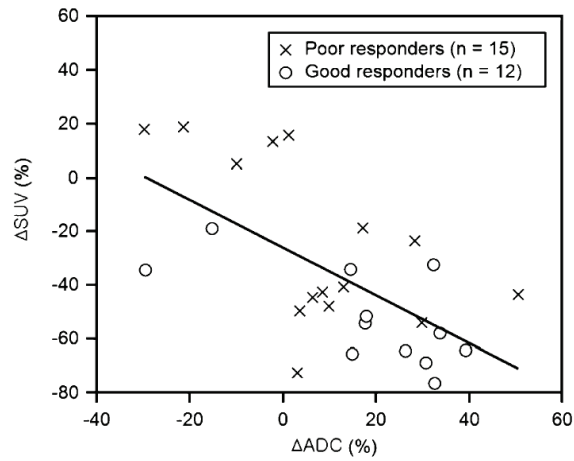


Figure 1. Relationship between Δ SUV and Δ ADC after chemotherapy in patients with osteosarcoma^[2]

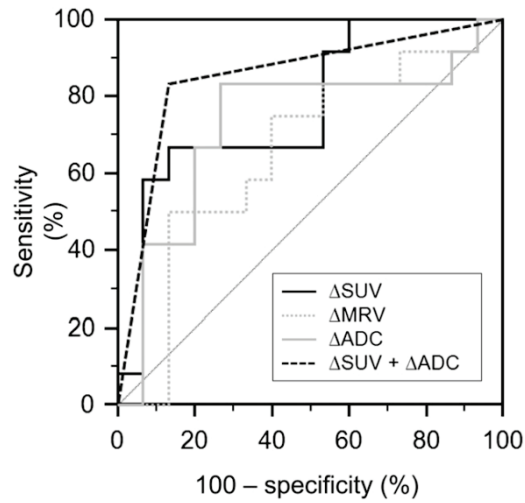


Figure 2. ROC analysis with Δ SUV, Δ MRV, Δ ADC, and combined use of Δ SUV and Δ ADC in patients with osteosarcoma^[2]

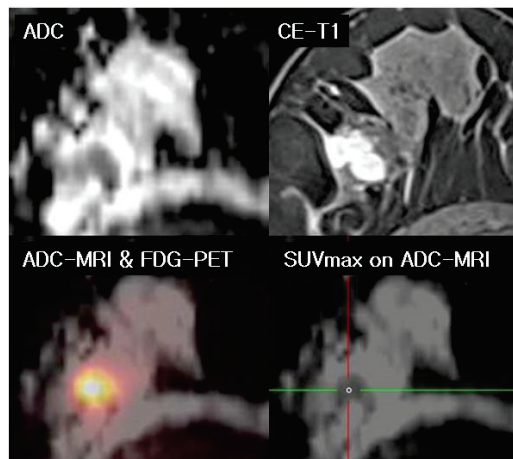


Figure 3. MRI and PET images and placement of ROI in a case of patient with breast cancer^[3]

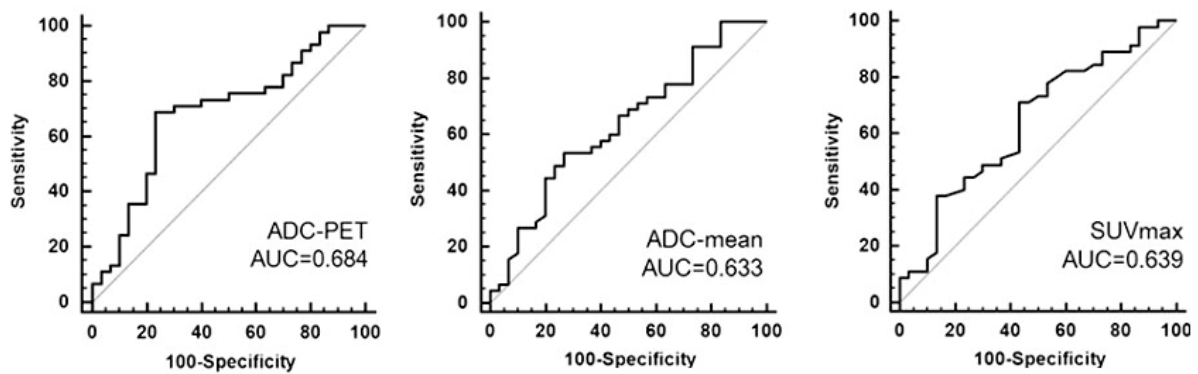


Figure 4. Comparison of ROC curves with ADC-PET, ADC only and PET only in patients with breast cancer^[3]

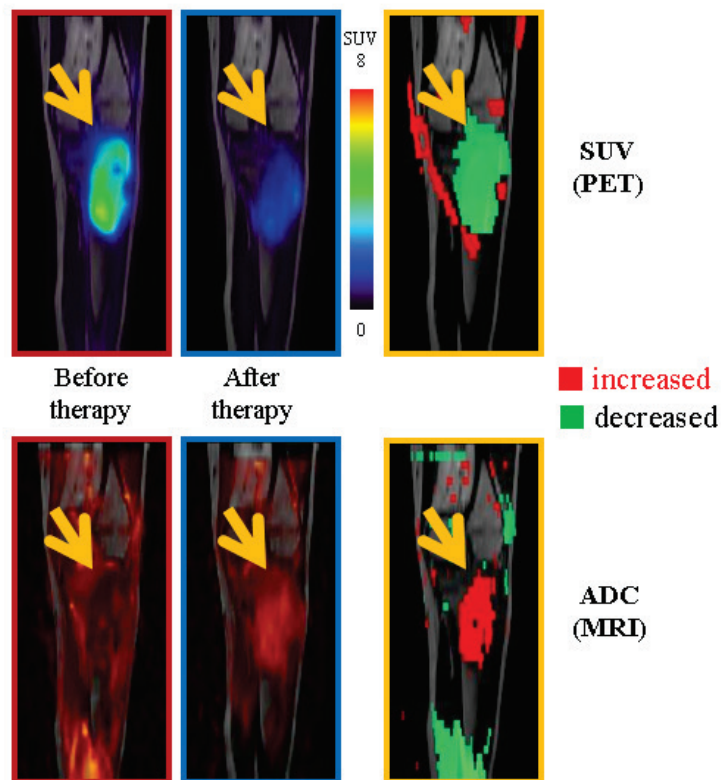


Figure 5. Voxel-based maps of Δ SUV and Δ ADC to discriminate therapeutic response in a patient with osteosarcoma

4. Discussion and Conclusion

As many clinicians and researchers has expected, the combined use of multi-functional image conventionally obtained from PET and MRI of functional PET and MRI showed better performance in differentiation of tumor grading and therapy response. In addition to ADC values, other functional MR techniques such as dynamic contrast enhanced MR and spectroscopy also can provide further information required to more precise evaluation of tumor status, with combining various functional PET imaging

techniques. In special, recent development of simultaneous PET/MRI system have big potential to promote the development and application of new strategies for clinical research and diagnosis using multi-dimensional and multi-parametric analysis.

Acknowledgments

This work was supported by Establishment of Center for PET Application Technology Development, Korea Institute of Radiological and Medical Sciences (KIRAMS)

References

- [1] B.M. Ellingson, M.G. Malkin, S.D. Rand, et al., "Validation of functional diffusion maps as a biomarker for human glioma cellularity," *J Magn. Reson. Imaging.*,31, pp.538-548, 2010
- [2] B.H. Byun, C.B. Kong, I. Lim, et al., " Combination of ¹⁸F-FDG PET/CT and diffusion-weighted MR imaging as a predictor of histologic response to neoadjuvant chemotherapy: preliminary results in osteosarcoma," *J Nucl Med.*, 54, pp.1053-1059, 2013.
- [3] B.H. Byun, W.C. Noh, I. Lim, et al., " A new method for apparent diffusion coefficient measurement using sequential (18)F-FDG PET and MRI: correlation with histological grade of invasive ductal carcinoma of the breast.," *Ann Nucl Med.* 27, pp.720-728, 2013.

(11) Development of flexible experimental and image database system

Hiroshi Watabe

Cyclotron and Radioisotope Center, Tohoku University, Japan

Abstract

In medical imaging fields, hospital information system (HIS), radiology information system (RIS) and picture archiving and communication system (PACS) have long history and are well established infrastructure in hospital. Recent innovations for imaging equipment lead to molecular imaging in basic science, and researchers regularly utilize several imaging modalities such as PET, SPECT, optical imaging, MRI. However, due to conceptional differences for organizing data between daily hospital routines and molecular imaging studies, no conventional HIS/RIS/PACS systems fit the researchers' requisitions. We developed MIBASE, very flexible experimental and image database system for molecular imaging research. The MIBASE records all information regarding experiments such as subject conditions, experimental protocol, notification so on, and store acquired images by several imaging modalities. File formats stored in the MIBASE are arbitrary, and any image data will be exported to a PACS server by converting data of any format into DICOM format. The MIBASE can be accessed by any Web browser through Internet, thus, it is possible to remotely retrieve data and experimental records. Experimental records and images are shared among researchers who have participated experiments under a research group. Access control mechanism is also introduced to protect data owned by a group from other groups. The system runs on a Linux base workstation and most of software codes are written in Python script language with Pylons web framework. The MIBASE offers the infrastructure for molecular imaging researches, which results in well-organized data management and rapid achievement of scientific outcomes.

1. Introduction

Hospital information system (HIS), radiology information system (RIS) and picture archiving and communication system (PACS) have long history (since 1960's)[1,2] and nowadays it is considered a modern hospital should have these systems. Molecular imaging research is a research field which visualizes particular molecules inside a living organisms by means of several imaging modalities such as positron emission tomography (PET), single photon emission tomography (SPECT), optical imaging, magnetic resonance imaging (MRI) (Fig. 1). The molecular imaging is interdisciplinary field, in which many researchers from different backgrounds must cooperate, and it is important to share their knowledges and information to advance their research. Therefore, among molecular imaging researchers, there has been strong demands to have central image storage and information database. However, the conventional HIS/RIS/PACS do not fit their requisitions due to conceptional differences for organizing data between daily hospital routines and molecular imaging studies (Table 1). In addition, the

commercial HIS/RIS/PACS are very expensive for researchers of basic science. Our aim is to develop experimental and image database system which could be employed in molecular imaging research.

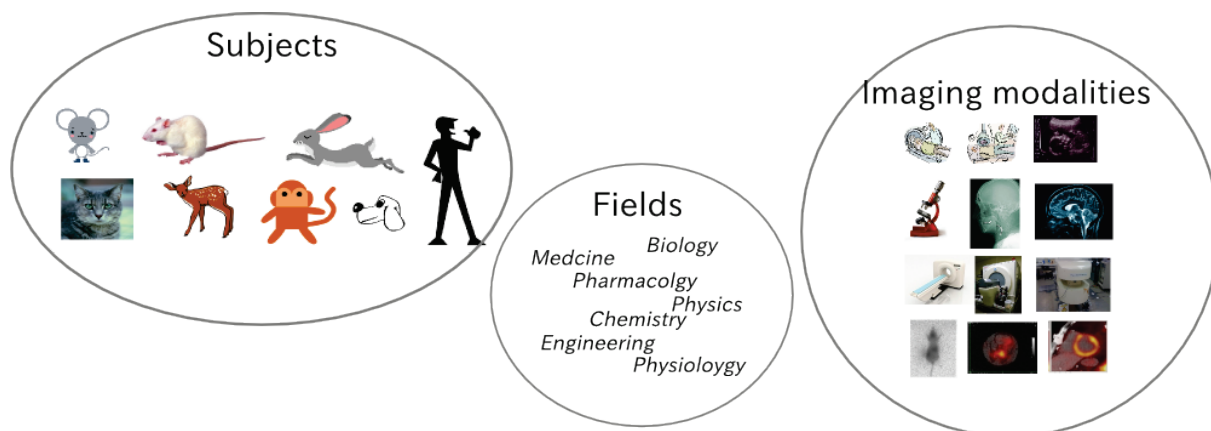


Figure 1 Molecular imaging research is a research involving several imaging modalities, target species and researchers who have different backgrounds.

Table 1: Comparisons between HIS/RIS/PACS and MIBASE

	HIS/RIS/PACS	MIBASE
Start point for data retrieve	a patient ID	a project ID
Examination	par a patient	possible to have several subjects with different species
Image file format	DICOM format	no restriction for image format
Data protection	share in all hospital staff	share in a particular group under a project

2. Methods

We developed MIBASE, experimental and image database system for molecular imaging research, which fulfills needs for molecular imaging studies and could be a substitute of HIS/RIS/PACS for molecular imaging research. The MIBASE is an integration system of both experimental and image databases. The users can store all information regarding experiments and store acquired image data by several imaging modalities. Unlike the imaging modalities installed in a hospital, not all image modalities for molecular imaging have capability to communicate by DICOM (digital image communication in medicine) standards, therefore, the MIBASE can store any image data with arbitrary format. The MIBASE is, then, possible to convert image data with different format to DICOM format and export to a PACS server. The MIBASE is a Web server which enable users using Web browsers to remotely access their data and records through Internet. By analyzing data format by the MIBASE, the users can access data stored in the MIBASE in proper way. For instance, the user will view image, play movie or listen sounds dependent on a file format. A research project is registered into the MIBASE, and users who involve this project can access all

experiments under this project (See Fig. 2). For each experiment, experimental records and image data from different imaging modalities are stored and shared among researchers who have participated experiments. Any kind of information regarding to the experiment such as experimental protocol, workflow, subject conditions, notification so on, can be collaboratively gathered as an electronic laboratory notebook [3]. Access control mechanism is also introduced to protect data owned by a group from other groups.

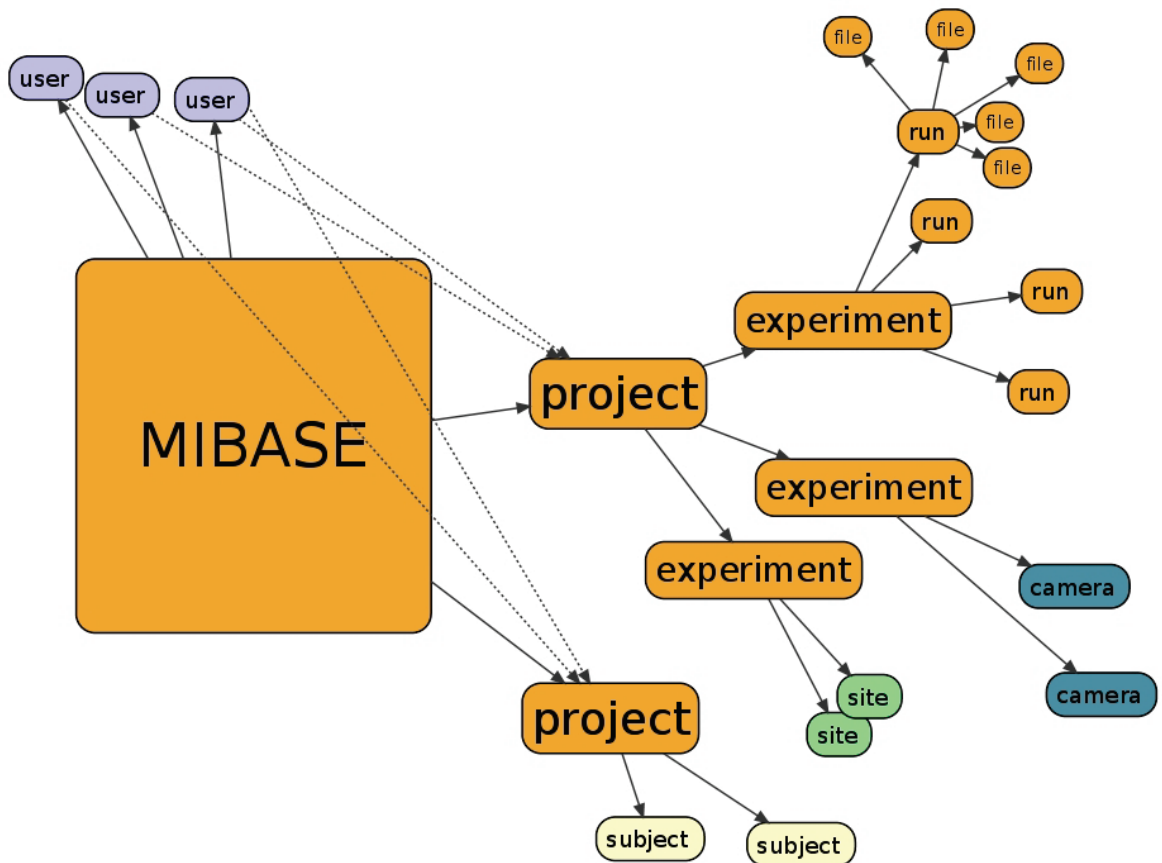


Figure 2 Database structure of MIBASE

2.1 System specifications

The system runs on a Linux base workstation (Intel Xeon CPU 2.93 GHz; 8 GBytes memory) and most of software codes are written in Python script language (Version 2.7) with Pylons web framework (Version 1.0). Some program codes such as image manipulation, data analysis are written in C language in order for fast computation. MySQL database engine (Version 5.1) is utilized as relational database (RDB). No propriety software are required.

2.2 Usages

As shown in Fig. 2, the MIBASE organizes data on a project base. By logging in the MIBASE, a user browses experiments under his/her own projects. One experiment sheet is created for each study. The animals employed in the study are registered to the experiment sheet. Each experiment sheet has several runs, and each run contains files related to the run. A run can be considered as an examination performed by

an imaging modality (Fig. 3). Contrary to an examination of a patient in a hospital, one run can be related to several subjects. Through a study, participants of the study write down any notifications and information in the experiment sheet to share with other participants. Data acquired during the study are stored in the run, and later a user can review the data using any Web browser or download the data from the MIBASE through any Web browser.





Runs						
Sequence	Camera		Time	Subjects	Description	Tag
1 (r3910)	iPET/MRI		edit 14:21:05 (2.0 min)	edit mouse-20121004-RGC6-1(s1278)	edit p-15,30,45,60(2min)	edit [C-11]Methionine
2 (r4759)	Inveon PET/CT		edit 16:00:00 (60.0 min)	edit mouse-20121004-RGC6-1(s1278)	edit	edit [F-18]FDG
3 (r4760)	eXplore Locus		edit 17:30:00 (30.0 min)	edit mouse-20121004-RGC6-2(s1279)	edit	edit
4 (r3911)	iPET/MRI		edit 14:49:22 (2.0 min)	edit mouse-20121004-RGC6-2(s1279)	edit p-15,30,45,60(2min)	edit [C-11]Methionine

Figure 3. An example of an experiment page in the MIBASE. Several images from different modalities can be stored.

3. Conclusions

The MIBASE offers the infrastructure for molecular imaging researches, which results in well-organized data management and rapid achievement of scientific outcomes.

References

- [1] A R Bakker. HIS, RIS, and PACS. *Computerized Medical Imaging and Graphics*, 15(3):157–60, 1991.
- [2] H.K. Huang, Medical imaging, PACS, and imaging informatics: retrospective. *Radiol Phys Technol* 7:5-24, 2014
- [3] James D Myers, Elena S Mendoza, and Bonnie L Hoopes. A collaborative electronic laboratory notebook. In *International Conference, Internet and Multimedia Systems and Applications*, August 2001.

Proceedings of the 3rd NIRS-SNU Workshop on Nuclear Medicine Imaging Science and Technology

Date of Publishing: March 28, 2014

Editing and Publication:

Taiga Yamaya

Molecular Imaging Center, National Institute of Radiological Sciences

4-9-1 Anagawa, Inage-ku, Chiba 263-8555, Japan

e-mail : jpet@nirs.go.jp

Printed in Japan

NIRS-M-269